Reconfigurable Hinged Kirigami Tessellations

AVIV SEGALL*, ETH Zurich, Switzerland
JING REN*, ETH Zurich, Switzerland
MARCEL PADILLA, ETH Zurich, Switzerland
OLGA SORKINE-HORNUNG, ETH Zurich, Switzerland

We present a computational framework for designing geometric metamaterials capable of approximating freeform 3D surfaces via rotationally deployable kirigami patterns. While prior inverse design methods typically rely on standard, well-studied patterns, such as equilateral triangles or quadrilaterals, we step back to examine the broader design space of the patterns themselves. Specifically, we derive principled rules to determine whether a given planar tiling can be cut into a rotationally deployable hinged kirigami structure with possible curvature adaptation. These insights allow us to generate and validate a broad family of novel tiling patterns beyond traditional examples. We further analyze two key deployment states of a general pattern: the commonly used maximal area expansion, and the maximal rotation angle reached just before face collisions occur, which we adopt as the default for inverse design as it allows for simple deployment in practice, i.e., rotating the faces to their natural limit. Finally, we solve the inverse problem: given a target 3D surface, we compute a *planar tiling* that, when cut and deployed to its maximal rotation angle, approximates the input geometry. We show that for a subset of patterns, the deployed configurations are hole-free, demonstrating that curvature can be achieved from planar sheets through local combinatorial changes. Our experiments, including physical fabrications, demonstrate the effectiveness of our approach and validate a wide range of previously unexplored patterns that are both physically realizable and geometrically expressive.

CCS Concepts: • **Computing methodologies** → **Shape modeling**.

Additional Key Words and Phrases: Computational fabrication, kirigami, surface approximation, metamaterials, inverse design

ACM Reference Format:
Aviv Segall, Jing Ren, Marcel Padilla, and Olga Sorkine-Hornung. 2025. Reconfigurable Hinged Kirigami Tessellations. In *SIGGRAPH Asia 2025 Conference Papers (SA Conference Papers '25), December 15–18, 2025, Hong Kong, HK, China.* ACM, New York, NY, USA, 18 pages. https://doi.org/10.1145/3757377.3763895

1 Introduction

The design of geometric metamaterials that transform flat sheets, such as paper, metal and fabric, into prescribed 3D shapes is a central challenge in computational fabrication. A key objective is to achieve programmable curvature by encoding geometric information into planar sheets to enable controlled deformation into target freeform surfaces. Various strategies have been developed to achieve this objective. Origami-based methods generate curvature through controlled folding, concealing excess material via crease patterns [Tachi 2008]. Smocking techniques, adapted from textile design, induce curvature by gathering excess fabric into pleats [Segall et al. 2024]. Kirigami-based methods create strategic cuts in the flat material, introducing holes to accommodate curvature [Konaković et al. 2018; Jiang et al. 2020, 2022]. Other methods leverage inflatable designs [Skouras et al. 2014; Jin et al. 2020; Panetta et al. 2021; Ren et al. 2024a; He et al. 2025] or grid shell structures [Panetta et al. 2019; Schikore et al. 2021; Becker et al. 2023; Liu et al. 2023] to achieve curvature during deployment.

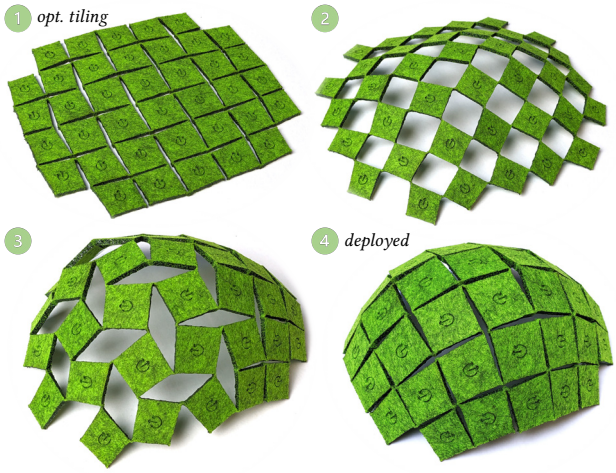

Fig. 1. The deployment of a closed hemispherical shape from a flat, gapless, optimized tiling (the computed tiling contains no gaps; the visible openings result from laser cutting). Engraved arrows help visualize local orientations.

Beyond these well established paradigms, there exists a less explored but powerful mechanism for achieving curvature: *local connectivity reconfiguration*. Through specific cuts, a *planar tiling* can be converted into a hinged kirigami structure, allowing its faces to rotate rigidly on hinge vertices. This approach enables programmable curvature to emerge from local combinatorial changes, as illustrated in Figures 1 and 2. Such hinged kirigami structures are often referred to as auxetic structures.

Prior work on hinged kirigami structures typically starts from a fixed, well-known pattern, such as a regular tessellation with equilateral triangles [Konaković et al. 2018] or squares [Jiang et al. 2022], and optimizes it for deployment at maximal area expansion, where holes introduced by cuts are opened to become as large as possible, allowing the structure to accommodate the prescribed curvatures. While effective, such methods are fundamentally limited by the expressive range of a standard pattern types and do not fully leverage the curvature potential that arises from connectivity

*joint first authors with equal contribution

Authors' Contact Information: Aviv Segall, ETH Zurich, Switzerland, aviv.segall@inf.ethz.ch; Jing Ren, ETH Zurich, Switzerland, jing.ren@inf.ethz.ch; Marcel Padilla, ETH Zurich, Switzerland, marcel.padilla@inf.ethz.ch; Olga Sorkine-Hornung, ETH Zurich, Switzerland, sorkine@inf.ethz.ch.



This work is licensed under a Creative Commons Attribution 4.0 International License.
SA Conference Papers '25, Hong Kong, HK, China
© 2025 Copyright held by the owner/author(s).
ACM ISBN 979-8-4007-2137-3/2025/12
https://doi.org/10.1145/3757377.3763895

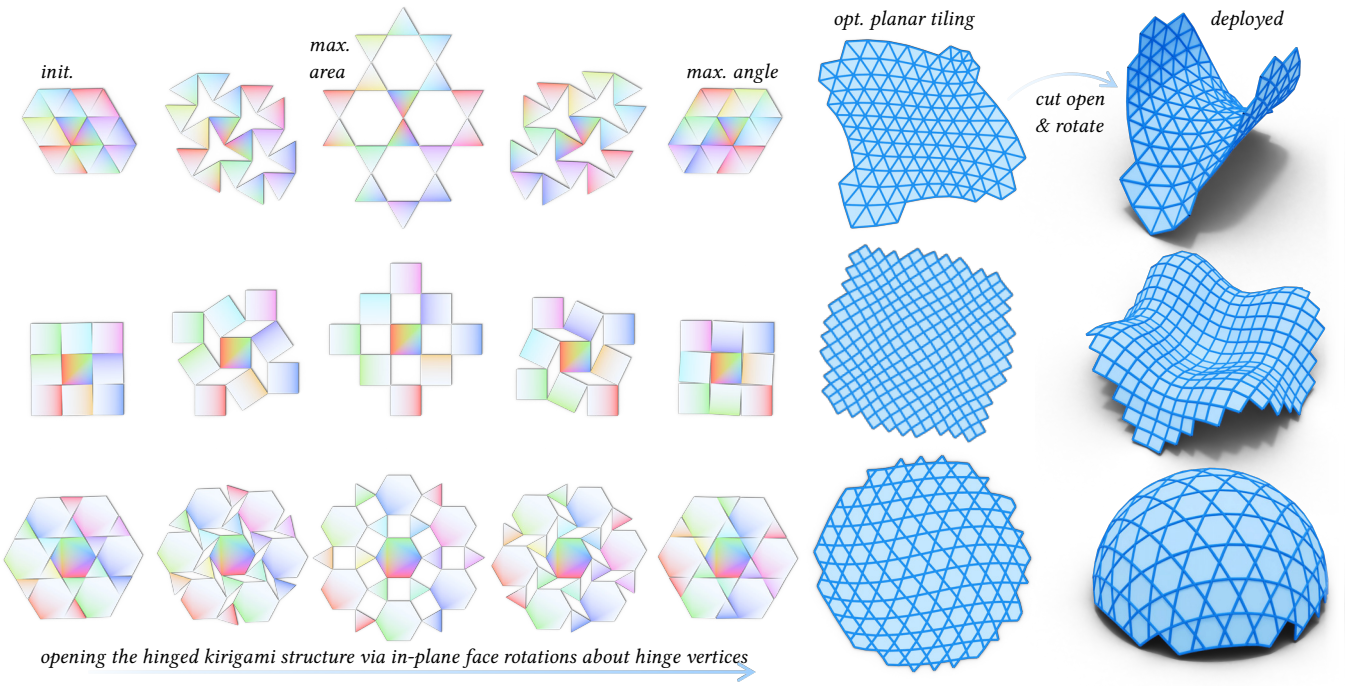

Fig. 2. A planar tiling mesh is cut along all interior edges, leaving specifically computed hinges at all vertices, such that the structure can be opened up and expanded in-plane (first five columns) or into a 3D shape (last two columns) solely via *rigid* transformations of the faces. The color gradients help visualize the rotations of the faces occurring during deployment. The three patterns in the first column have been explored in prior work on shape morphing: Konaković et al. [2018] and Jiang et al. [2022] studied the triangular pattern (first row) and quadrilateral pattern (second row), while the third-row pattern resembles a waving pattern shown in [Ren et al. 2021]. However, these works primarily focus on a single deployed state: the configuration with maximal area expansion during deployment (third column). In contrast, our work extends the deployment process to a second extreme: the configuration with maximal rotation angle (fifth column), beyond which face collisions occur. Moreover, we explicitly consider both the pre- and post-deployment configurations. This enables us to design fully closed, hole-free planar tilings (second-to-last column) that, when cut and deployed, achieve the target 3D freeform surface shapes (last column).

changes–those triggered at the maximal rotation angle where face collisions occur (e.g. in Fig. 2, fifth column). In this work, we explore the broader design space of planar tilings and address the challenge: Which tilings can be cut into rotationally deployable hinged kirigami structures that realize target curvatures through local combinatorial changes and hole formations when the hinged faces reach their rotational limits during deployment?

Our main contributions are: (1) We present a systematic study of the relationship between planar manifold tilings, kirigami patterns and metamaterial design. Specifically, we address the following fundamental question: Which planar tilings admit a valid cutting pattern such that the resulting hinged kirigami structure holds rotational freedom for deployment, which is commonly used in metamaterial design. (2) We propose an effective formulation and an efficient pipeline to design planar tilings, verify their validity for deriving a deployable hinged kirigami structure and simulate the deployment process of valid patterns. (3) We target two critical deployment configurations: maximal area expansion (achieving the largest projected coverage) and maximal rotation angle (beyond which face collisions occur), and mathematically characterize the latter. (4) We solve the inverse design problem by computing 2D tilings that, when cut and deployed to their maximal rotation angle, approximate target 3D surfaces.

2 Related work

Geometric metamaterials are a subset of mechanical metamaterials that can achieve complex geometric shapes through specific manipulations. These manipulations include *folding* flat sheet materials such as paper or metal, commonly known as origami [Wei et al. 2013; Dudte et al. 2016; Narumi et al. 2023], *cutting* flat sheets with interconnected hinges (a technique often regarded as a subset of kirigami) [Konaković et al. 2016, 2018; Choi et al. 2019; An et al. 2020; Dang et al. 2021; Jiang et al. 2022] and *stitching* [Segall et al. 2024; Chang et al. 2024]. Geometric metamaterials are typically characterized by periodic tessellations of simple shapes, such as triangles [Konaković et al. 2016, 2018; Chen et al. 2021; Koh et al. 2023], quadrilaterals [Wang et al. 2017; Rafsanjani and Bertoldi 2017; Celli et al. 2018; Choi et al. 2019; Jin et al. 2020; Jiang et al. 2022; Dudte et al. 2023] and hexagons [Castle et al. 2014, 2016], as well as more intricate and complex patterns [Rafsanjani and Pasini 2016; Malomo et al. 2018; Segall et al. 2024]. These tessellations can be computationally designed or modified to achieve target 3D geometric shapes, often via an inverse design problem formulation.

Our work is inspired by Konaković et al. [2018] and Jiang et al. [2022] and focuses on a similar problem: designing *rigid* kirigami-based geometric metamaterials. Konaković et al. [2018] focus on optimizing triangular auxetic patterns using conformal mappings,

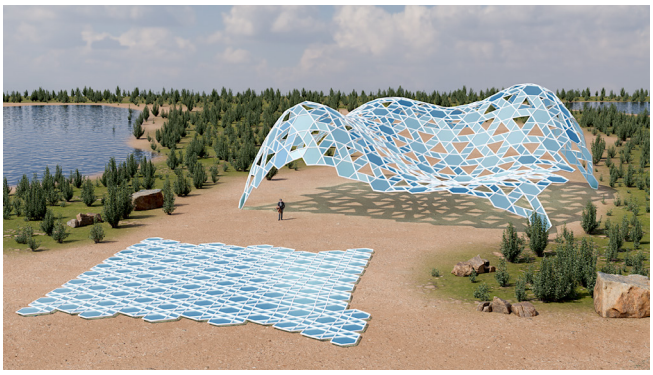

Fig. 3. Potential application in architecture: The target structure can be fabricated flat, in one piece without gaps or holes (*left*). Joints could be locally installed and rotated, altering connectivity and inducing curvature, thus allowing the design to deploy seamlessly into its final 3D form (*right*).

attaining target curvatures at *full expansion* starting from a semi-closed configuration. Jiang et al. [2022] focus on optimizing quadrilateral patterns based on the principal stretch directions, achieving target curvatures at full expansion starting from a fully-closed configuration (gap-free). We aim to develop a more general framework capable of handling diverse kirigami patterns. In many cases, these patterns lack analytic solutions for describing their full expansion, and the expansion or closing process might *not* follow a conformal deformation as in [Konaković et al. 2018], nor maintain a fixed ratio between the principal stretch directions as in [Jiang et al. 2022].

Reconfigurable metamaterials. While geometric metamaterials are primarily focused on achieving specific target 3D shapes at the *final* deployment stage, reconfigurable metamaterials also take into account additional aspects of the deployment process, including the initial geometry (e.g., fully closed) [Jiang et al. 2022; Dudte et al. 2023], intermediate geometric shapes [Tang et al. 2019; Dang et al. 2022; Dudte et al. 2023], mechanisms [Jiang et al. 2022, 2024; Liu et al. 2024], material properties [Tang and Yin 2017; Yang et al. 2018; Gu et al. 2024] and mechanical properties [Lee et al. 2012; Schenk and Guest 2013; Ma et al. 2018] during transformations. Among reconfigurable metamaterials, those exhibiting mechanical bistability have gained significant attention due to their ability to achieve rapid changes in shape or functionality [Rafsanjani and Pasini 2016; Chen et al. 2021; Jiang et al. 2022; Koh et al. 2023]. The closest related to ours is by Dudte et al. [2023], who propose a computational method for constructing non-manifold *quad* patterns that exhibit two fully closed states, each approximating a given *2D* shape contour. We extend their work in two key directions: (1) Our method generalizes to a broader class of kirigami patterns, including those inspired by origami [Tachi 2013], smocking [Ren et al. 2024b; Segall et al. 2024], or derived from planar tilings, and (2) our method enables the realization of 3D curved shapes, broadening the design space and practical applications.

Inverse design. Recent advancements in computational fabrication have explored a wide range of techniques for creating complex

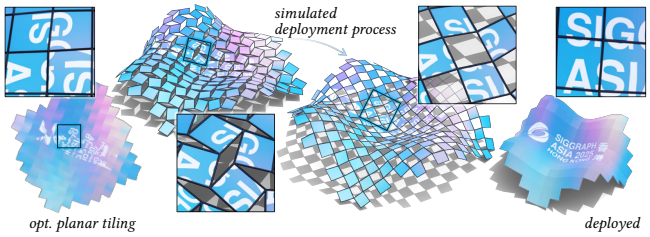

Fig. 4. A textured 3D puzzle, deployed from a flat configuration.

3D geometric structures using various materials, including *fabric* [Zhang et al. 2019; Jourdan et al. 2020; Segall et al. 2024; Chang et al. 2024], *yarns* [Narayanan et al. 2018; Wu et al. 2019; Edelstein et al. 2022], *inflatable materials* [Skouras et al. 2014; Jin et al. 2020; Panetta et al. 2021; Ren et al. 2024a], *developable materials* such as paper and metal sheets [Demaine and Tachi 2017; Callens and Zadpoor 2018; Stein et al. 2018; Jiang et al. 2020; Ion et al. 2020; Binninger et al. 2021; Zhao et al. 2022; Narumi et al. 2023; He et al. 2024] *stretchable materials* [Jourdan et al. 2022; Guseinov et al. 2017; Shimoda et al. 2023] and *auxetic materials* [Konaković et al. 2016, 2018; Chen et al. 2021; Jiang et al. 2022]. Target shapes or curvatures can be actuated through various methods, such as *heat* [Jourdan et al. 2023; Narumi et al. 2023; Koh et al. 2023; Chen et al. 2024; Walker and Shea 2024], *tension* [Guseinov et al. 2017; Pérez et al. 2017], *bending* [Pérez et al. 2015; Kilian et al. 2017; Panetta et al. 2019; Ren et al. 2022; Becker et al. 2023; Liu et al. 2023; Becker et al. 2024; Ono et al. 2024], and *gravity* [Chen et al. 2014; Malomo et al. 2018; Zhang et al. 2019]. While these techniques often rely on physical simulation, another popular direction involves geometric solutions with computationally prescribed curvatures [Dudte et al. 2016; Konaković et al. 2018; Choi et al. 2019; Jiang et al. 2020, 2022; Segall et al. 2024]. Our work falls within the realm of *geometry-based inverse design*, where the fabrication is achieved using solid materials connected with joints, without additional actuation steps. Similar to other reconfigurable structures [Kusupati et al. 2023; Becker et al. 2024], our reconfigurable kirigami design is cost-effective thanks to its minimal material waste: prior to deployment, the structure forms a planar tiling without holes or gaps, eliminating the need to remove excess material.

3 Background

3.1 Definitions & notation

A *planar tiling* (either periodic or aperiodic) is an arrangement of geometric shapes (typically polygons) that fully covers a planar region without overlaps or gaps, e.g., see Fig. 6 (a). We refer to a 2D manifold polygonal mesh with disk topology as a tiling to emphasize that the mesh contains no holes. We denote the mesh (tiling) as $\mathcal{T} = (\mathcal{V}, \mathcal{F})$, where $\mathcal{V}$ is the set of vertices, and $\mathcal{F}$ is the list of planar polygonal faces. A *complete cut* of tiling $\mathcal{T}$, denoted $\mathcal{E}_c$, is a set of *directed* edges that covers *all interior* edges of $\mathcal{T}$ (see Fig. 6 (b)). For an interior edge e of $\mathcal{T}$, let $\vec{e}$ denote its associated directed cut edge in $\mathcal{E}_c$, where the direction determines the placement of the hinge. For example, consider an interior edge $(v_1, v_2) = f_i \cap f_j$ shared by two faces f_i and f_j. If the associated directed cut edge in $\mathcal{E}_c$ is $\vec{e} = (v_1 \rightarrow v_2)$, then after applying the cut, a duplicated

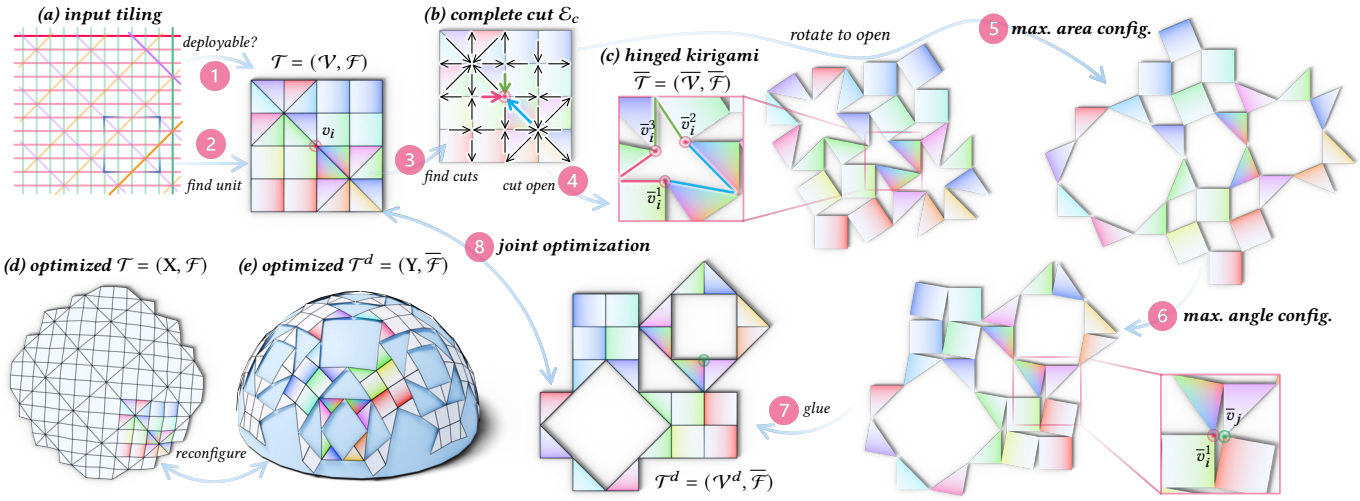

Fig. 5. **Method overview**. Given a planar tiling (a), our method first determines whether the tiling is deployable (step ①), Sec. 4.1). If deployable, we identify the unit tile (step ②, Sec. 4.2), apply the complete cut $\mathcal{E}_c$, defined in Sec. 3.1 (step ③) to create a hinged kirigami structure, defined in Sec. 3.1 (step ④) and simulate its deployment process. The pattern first reaches its maximal area expansion configuration (step ⑤), then continues to its maximal rotation angle configuration (step ⑥). Beyond this point, further deployment would cause face collisions, so the maximal angle configuration is selected as the final deployed state. In this deployed configuration, we merge co-located vertices (step ⑦), resulting in a new mesh $\mathcal{T}^d$. Finally, we jointly optimize the initial configuration $\mathcal{T}$ and the deployed configuration $\mathcal{T}^d$, constraining $\mathcal{T}$ to remain planar and $\mathcal{T}^d$ to approximate a target 3D geometry while preserving reconfigurability between the two: both configurations share the same set of faces, arranged differently (step ⑧, Sec. 4.3).

edge $\overline{e}$ is created, emanating from the same source vertex. As a result, the faces f_i and f_j are no longer connected along the edge, but instead hinge at the source vertex. See the blue/red arrows in Fig. 6 (b,c). Applying the complete cut $\mathcal{E}_c$ to the tiling $\mathcal{T}$ yields a new, non-manifold 2D polygonal mesh $\overline{\mathcal{T}} = (\overline{\mathcal{V}}, \overline{\mathcal{F}})$, where $\overline{\mathcal{V}}$ includes the original vertices $\mathcal{V}$ and their duplicates induced by the cuts, and $\overline{\mathcal{F}}$ retains the same geometric shapes as $\mathcal{F}$ in one-to-one correspondence but with updated vertex indices due to the altered connectivity. Since a complete cut $\mathcal{E}_c$ covers all interior edges of $\mathcal{T}$ by definition, applying it yields a structure where all faces are connected solely by hinge vertices, with no shared edges between them. We say that a tiling $\mathcal{T}$ admits a *hinged kirigami structure* if there exists a complete cut $\mathcal{E}_c$ such that in the resulting mesh $\overline{\mathcal{T}}$, every vertex that originates from an interior vertex in $\mathcal{T}$ is shared by exactly two faces in $\overline{\mathcal{T}}$. See Figures 5 and 6 for examples of hinged kirigami structures.

Definition 3.1 (Deployability). A hinged kirigami pattern is *deployable* if its faces can rotate rigidly around hinge vertices without collision with neighboring faces. We call a tiling *deployable* if it admits a deployable hinged kirigami structure. We call the angle between the duplicated edges e and $\overline{e}$ after cutting the *opening angle*, denoted as θ_e (see Fig. 6 (c)). We call a deployable tiling *uniformly* deployable if the opening angles of all interior edges are equal to each other in every deployment configuration.

3.2 Problem formulation

Our work bridges kirigami, auxetic metamaterials and computational design by addressing three core challenges.

Problem 3.1 (Deployability of tilings). How can we determine whether a tiling is deployable, i.e., whether there exists a complete cut that transforms the tiling into a hinged kirigami structure whose faces can rotate *rigidly* about hinge vertices without collision?

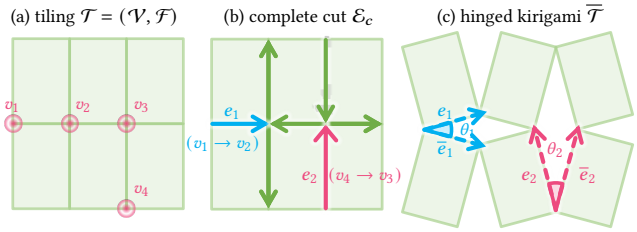

Fig. 6. *Left*: a manifold tiling $\mathcal{T}$ with vertices $\mathcal{V}$ and (polygonal) faces $\mathcal{F}$. *Middle*: an example complete cut $\mathcal{E}_c$ (highlighted by arrows), i.e., a set of directed edges covering all interior edges in $\mathcal{T}$. *Right*: the hinged kirigami structure $\overline{\mathcal{T}}$, obtained by applying the complete cut $\mathcal{E}_c$ to the tiling $\mathcal{T}$. Each directed cut edge $e = (v_i \to v_j)$ creates a duplicated edge $\overline{e}$ that emanates from the same vertex as e (with an associated opening angle θ_e), such that the two neighboring faces of e hinge at this vertex.

Problem 3.2 (Rotational deployment analysis). Given a deployable hinged kirigami pattern, how can we mathematically characterize the bounds of face rotations about hinges, i.e., its opening angles, that define its maximally open configurations during deployment?

Observation 3.1. A deployable hinged kirigami pattern typically admits two distinct maximally open configurations during deployment: (1) **maximal area expansion**, where the pattern achieves its largest projected coverage area, and (2) **maximal rotation angle**, beyond which further rotation would cause face collisions.

Problem 3.3 (Inverse design). How can we computationally modify a 2D manifold tiling such that, when cut and rotated to the maximal opening angle, it achieves a desired 3D geometry?

State-of-the-art analysis. Problems 3.2 and 3.3 have been partially addressed for specific standard patterns with well-defined maximal area expansion configurations. For example, the regular equilateral triangular pattern studied in [Konaković et al. 2016, 2018] achieves maximal area expansion when neighboring hinge vertices become *concyclic*, as its deployment follows a conformal transformation. The quadrilateral pattern studied in [Jiang et al. 2022] reaches maximal area expansion when adjacent faces form *right angles* at hinge vertices. While these observations enable effective inverse design solutions, critical gaps remain: (1) Existing methods ignore maximal opening angle configurations, which significantly enrich the design space and provide intuitive deployment guidance, namely, rotating until face collision occurs, rather than targeting specific geometric conditions like concyclic positions or right angles. (2) The optimized patterns contain gaps in their "closed" state (before deployment), leading to material waste and increased manufacturing complexity. On the other hand, Dudte et al. [2023] are, to our knowledge, the first to examine both maximal area expansion and maximal opening angle configurations in non-manifold quadrilateral patterns. However, their work only addresses inverse design for 2D contour approximation, leaving the more challenging 3D shape realization unsolved. Consequently, neither Problem 3.2 nor Problem 3.3 has been fully resolved for conventional regular patterns.

Challenges. We address the key questions formulated in Problems 3.1, 3.2 and 3.3 for general tilings like the one shown in Fig. 5. These patterns raise three fundamental challenges: (1) determining whether a complete cut exists that ensures connectivity and enables deployability in the resulting hinged kirigami structure, (2) mathematically characterizing their maximally open configurations in terms of area expansion and rotation angle, and (3) ensuring a gap-free closed state before deployment in inverse-designed patterns. Note that maximally open configurations typically lack analytic solutions, and the maximal rotation angle configurations often retain holes, see e.g. Figures 3 and 5.

4 Method

To address the aforementioned challenges, we first develop principled rules to determine the existence of a complete cut on a given 2D manifold tiling (see Sec. 4.1). Next, we quantify the maximally open states (w.r.t. area expansion and opening angle) of the hinged kirigami structure formed by the unit tile and its immediate neighbors extracted from the input tiling (see Sec. 4.2). These building blocks enable inverse design of planar tilings that achieve target curvatures upon deployment (see Sec. 4.3).

4.1 Constructing hinged kirigami structures from tilings

To address Problem 3.1, i.e., deriving a deployable hinged kirigami structure from a given planar tiling represented as a manifold mesh $\mathcal{T} = (\mathcal{V}, \mathcal{F})$, the input tiling must satisfy the following conditions: (1) **Combinatorial condition**: there exists a complete cut $\mathcal{E}_c$ such that in the resulting hinged mesh $\overline{\mathcal{T}} = (\overline{\mathcal{V}}, \overline{\mathcal{F}})$, each vertex in $\overline{\mathcal{V}}$ originating from an interior vertex of $\mathcal{T}$ is shared by exactly two faces. (2) **Geometric condition**: the complete cut $\mathcal{E}_c$ enables deployability of $\overline{\mathcal{T}}$, i.e., it permits faces to rigidly rotate by a non-zero angle around hinge vertices without collision.

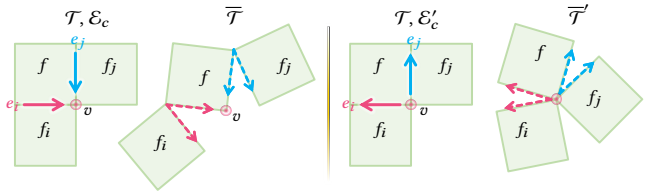

Fig. 7. Consider face f of tiling $\mathcal{T}$, let its two neighboring faces f_i and f_j share a common vertex v via edges e_i and e_j. The cuts assigned to e_i and e_j in the complete cut $\mathcal{E}_c$ must have alternating directions. If both cuts point into (*left*, $\mathcal{E}_c$) or away (*right*, $\mathcal{E}'_c$) from v, the resulting structure violates the hinged kirigami condition–either leaving a dangling vertex v (*left*, $\overline{\mathcal{T}}$) or connecting more than two faces at v (*right*, $\overline{\mathcal{T}}'$).

Recall the definition of a cut: given an edge (v_1, v_2) shared by faces f_i and f_j, if its associated cut is directed as $(v_1 \rightarrow v_2)$, the resulting structure contains a duplicated edge emanating from the same vertex, causing the two faces to hinge at that source vertex. From this, we conclude that two *adjacent* cut edges, belonging to the same face and sharing a vertex v, must have different directions at v, i.e., one cut edge starts at v and the other ends at v. Otherwise, the resulting cut structure would either contain a dangling vertex or cause a vertex to be shared by more than two faces, violating the definition of a hinged kirigami structure. See Fig. 7 for examples of violations of this condition. Therefore, checking the combinatorial condition reduces to a graph problem: does the tiling admit a complete cut such that every pair of adjacent cut edges has alternating directions? This is equivalent to the 2-colorability of the dual graph of the tiling. The dual is a planar graph, which means it is 2-colorable, or bipartite, *if and only if* all its faces (dual of vertices) consist of an even number of edges [Bandelt et al. 2010]. This leads to the following observation:

Remark 4.1. A planar manifold tiling can be cut into a valid hinged kirigami pattern *if and only if* all its interior vertices have *even* valency.

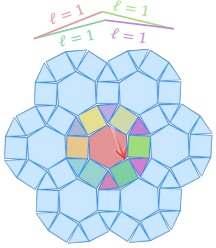

Fig. 8. Non-deployable

We can therefore verify the *combinatorial* condition for deployability by checking whether all interior vertex valences are even. Satisfying this condition guarantees the existence of a complete cut where adjacent cut edges at every vertex *alternate* in direction, without violations like those shown in Fig. 7, resulting in a valid hinged kirigami structure. This valid complete cut $\mathcal{E}_c$ is fully determined, up to reversal of all cut directions. See Sec. A in the supplementary material for details on its construction. While even vertex valency guarantees valid *combinatorial* connectivity after cutting, it does *not* ensure *geometric* rotational freedom in the resulting structure. Fig. 8 shows a tiling that satisfies the even-valency condition but still suffers face collisions during attempted rotation, resulting in a kirigami structure that is not deployable in the plane.

Definition 4.1 (Deployment-friendly vertex). Let $\mathcal{T} = (\mathcal{V}, \mathcal{F})$ be a planar tiling with a complete cut $\mathcal{E}_c$. Let $v \in \mathcal{V}$ be a vertex of even valency $2k$. Denote by $\vec{e}_1, \cdots, \vec{e}_k$ the directed edges (cuts) in

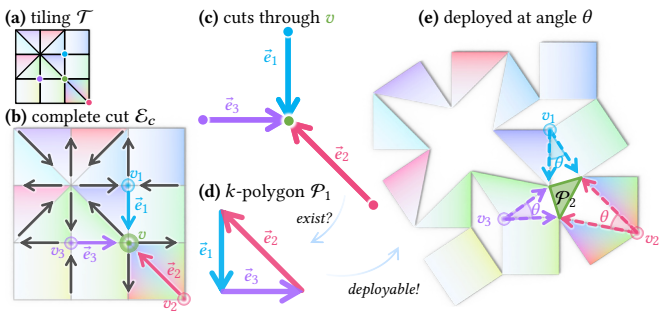

Fig. 9. We show a complete cut $\mathcal{E}_c$ (arrows in (b)) applied to the tiling in (a). The vertex v is 6-valent, with three incident cut edges $\vec{e}_1, \vec{e}_2, \vec{e}_3$ ending at v, highlighted in (c). In (d), we check whether a triangle $\mathcal{P}_1$ can be formed by translating the cut vectors $\vec{e}_i$, which is equivalent to verifying that $\sum_{i=1}^{3} \vec{e}_i = \vec{0}$. If such a $\mathcal{P}_1$ exists (i.e., the equality holds), v is deployment-friendly. If all vertices are deployment friendly, the tiling is deployable (e). Moreover, the polygon $\mathcal{P}_2$ formed by the duplicates of v is similar to $\mathcal{P}_1$, and the opening angles are equal (more details in Sec. B).

$\mathcal{E}_c$ ending at v, ordered cyclically. Vertex v is said to be *deployment-friendly* if $\sum_{i=1}^{k} \vec{e}_i = \vec{0}$. Refer to Fig. 9 for notation.

Proposition 4.1 (Necessary and sufficient condition for uniform deployability). For a planar tiling with all interior vertices of even valency, the following are equivalent: (1) Every interior vertex in the tiling is deployment-friendly. (2) The resulting hinged kirigami structure is uniformly deployable in 2D.

Sec. B of the supplementary materials presents a proof by construction. In brief, we show that for a deployment-friendly vertex, after cutting its incident edges, there exists a configuration of its neighboring faces where all opening angles are equal and non-zero, and all faces maintain their exact original geometry without deformation. In other words, we can realize a deployment state at this uniform opening angle.

Constructing uniformly deployable tilings. Prop. 4.1 lets us determine whether a tiling is uniformly deployable. Based on this, we build a user interface that synthesizes periodic tilings and checks deployment friendliness at each vertex. Users can define families of *parallel* lines by selecting three points on a regular triangle or quad grid: the first two specify the base direction, and the third determines the offset for generating parallel duplicates (see the supplementary video). Intersections of these line families naturally produce even-valency vertices, so the system only needs to check whether each vertex is deployment-friendly. Deployment-unfriendly vertices are highlighted in the UI (see Fig. 10, (a)). If all vertices pass, the system animates the deployment of the resulting hinged kirigami structure. This tool enables rapid exploration of novel, deployable tiling designs (e.g., see Figures 5 and 13).

4.2 Maximally open configurations

Given a periodic tiling $\mathcal{T}$ generated by a finite set of parallel line families that satisfy the deployability condition (Def. 4.1), we analyze its deployment behavior after introducing cuts. Our method consists of two main stages: (1) We first determine the unit tile, defined as the smallest region whose translational repetition reconstructs the

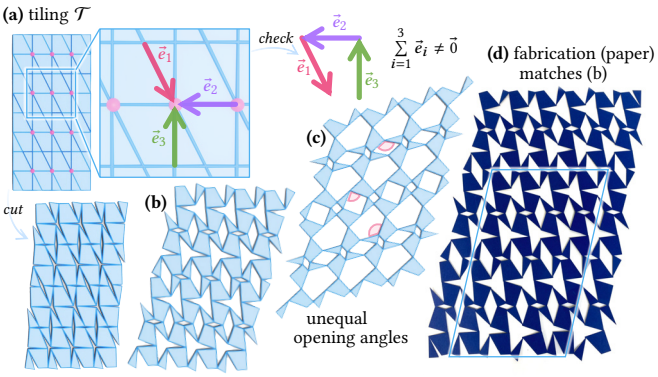

Fig. 10. (a) A tiling containing deployment-unfriendly vertices (highlighted in red) can still be deployable (b,c). However, as shown in (c), the opening angles are unequal. Consequently, the deployment is no longer a one-parameter family and cannot be computed analytically: opening angles must be optimized at each deployment state. In (b) and (d) we show a simulated and a fabricated result at a similar deployment stage. See further discussion in Sec. C in the supplementary material.

entire tiling $\mathcal{T}$. (2) We then analyze the deployment kinematics of the unit tile with its adjacent tiles. This localized analysis is sufficient to determine both maximally deployed configurations (w.r.t. area expansion and opening angles) and enables the systematic generation of arbitrary-scale deployed patterns without simulating the entire structure.

Identifying the unit tile. Given a set of distinct parallel line families $\mathcal{L} = \{\ell_i\}$, each family $\ell_i = (\mathbf{p}_i, \mathbf{q}_i, d_i)$ is defined by a base line passing through two distinct points $\mathbf{p}_i$ and $\mathbf{q}_i$, along with its infinite parallel replicas offset along the normal direction to $(\mathbf{p}_i - \mathbf{q}_i)$ by a distance of kd_i, where $k \in \mathbb{Z}$. To generate a valid tiling, the set $\mathcal{L}$ must contain at least two line families whose base lines are not parallel. Without loss of generality, we assume the first two families $\ell_1 = (\mathbf{p}_1, \mathbf{q}_1, d_1)$ and $\ell_2 = (\mathbf{p}_2, \mathbf{q}_2, d_2)$ satisfy the condition that their direction vectors are not parallel, i.e., $(\mathbf{q}_1 - \mathbf{p}_1) \nparallel (\mathbf{q}_2 - \mathbf{p}_2)$. Denote the intersection of the base line of ℓ_1 and ℓ_2 as $\mathbf{o}$, and the unit line direction $\mathbf{t}_i = (\mathbf{q_i} - \mathbf{p}_i)/\|\mathbf{q_i} - \mathbf{p}_i\|, i = 1, 2$. To determine the periodicity, we only need to compute the distances along the directions $\mathbf{t}_1$ and $\mathbf{t}_2$, denoted as λ_1 and λ_2, respectively, such that translations by $\lambda_1\mathbf{t}_1$ and $\lambda_2\mathbf{t}_2$ preserve all line intersections within $\mathcal{L}$. See Sec. D of the supplementary for detailed discussions.

Deployment analysis. We construct a 2-by-2 repetition of the unit tile, denoted as $\mathcal{T}_0$, and cut it open into a hinged kirigami structure $\overline{\mathcal{T}}_0$. According to Prop. 4.1, if all vertices in $\mathcal{T}_0$ are deployment-friendly, we know $\overline{\mathcal{T}}_0$ is uniformly deployable. That is, at any deployment state, the opening angles remain equal. This uniformity allows us to parameterize the entire deployment process using a single variable: the opening angle θ. We can optimize θ to maximize the area of the open kirigami pattern $\overline{\mathcal{T}}_0$, accounting both for faces in the tiling and holes induced by cuts. While this maximum area configuration is commonly used in prior works for deployment, we instead choose the configuration at the maximum opening angle. Consider a hinge vertex v shared by two faces f_i and f_j. Let α_i and α_j denote the internal angles at v for these two faces. The maximum

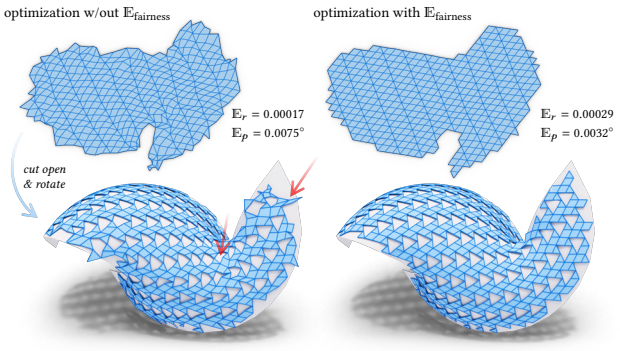

Fig. 11. Optimized tilings before (*top*) and after (*bottom*, overlaid with the target shape) deployment. *Left*/*right* sides compare results without/with the fairness term. Both patterns are fabricable, with low unsquared reconfigurability error ($\mathbb{E}_r$) and planarity error ($\mathbb{E}_p$) in degrees. Adding the fairness term helps preserve the shape of underconstrained boundary regions and holes. Red arrows highlight artifacts in the unregularized result.

opening angle allowed at v is $(2\pi - \alpha_i - \alpha_j)$. Rotating beyond this limit causes the faces to collide from the backside. Hence, the global maximum opening angle for the entire tiling is the minimum of these local vertex bounds, denoted as $\theta_{\max}$; beyond this threshold, collisions are inevitable. In this work, we define the deployment state using this maximum opening angle. It avoids optimization overhead and yields a simple instruction for practical deployment: rotate each face until a limit is reached. For any opening angle $\theta \in [0, \theta_{\max}]$, we compute the deployed state by starting from a seed face, rotating its neighbors by θ around their shared hinge vertices, and propagating this rotation face by face through the hinged kirigami structure.

4.3 Inverse design framework

For a chosen uniformly deployable tiling $\mathcal{T} = (\mathcal{V}, \mathcal{F})$, we can compute its deployed 2D configuration $\mathcal{T}^d = (\mathcal{V}^d, \overline{\mathcal{F}})$. Recall that $\mathcal{F}$ and $\overline{\mathcal{F}}$ are in one-to-one correspondence and share identical geometry. In essence, $\mathcal{T}$ and $\mathcal{T}^d$ consist of the same set of faces, merely rearranged. Given a target freeform 3D shape $\mathcal{M}$, our goal is to modify the 2D tiling $\mathcal{T}$, i.e., to solve for a new 2D embedding $\mathbf{X} \subset \mathbb{R}^2$, such that, after deployment (i.e., rotating each face to its maximal allowed angle), the resulting configuration $\mathcal{T}^d$ becomes a 3D embedding $\mathbf{Y} \subset \mathbb{R}^3$ that closely approximates the geometry of $\mathcal{M}$. In this step, we fuse co-located vertices in $\mathcal{V}^d$ (see Fig. 5 step ⑦), eliminating the need for a regularizer to keep them aligned during deployment optimization. Denote $n = |\mathcal{V}|$ and $m = |\mathcal{V}^d|$. We propose to jointly optimize both $\mathbf{X}$ and $\mathbf{Y}$:

$$\min_{\mathbf{X}\in\mathbb{R}^{n\times 2},\ \mathbf{Y}\in\mathbb{R}^{m\times 3}} \omega_1 \mathbb{E}_{\text{reconfig}}(\mathbf{X}, \mathbf{Y}) + \omega_2 \mathbb{E}_{\text{planar}}(\mathbf{Y}) + \tag{1}$$

$$\omega_3 \mathbb{E}_{\text{shape}}(\mathbf{Y} \mid \mathcal{M}) + \omega_4 \mathbb{E}_{\text{fairness}}(\mathbf{Y}). \tag{2}$$

The **reconfigurability** term penalizes distance distortions between all vertex pairs within each face, ensuring that the geometry of the faces remains identical before and after deployment during the optimization process. Denote by $\overline{f} \in \overline{\mathcal{F}}$ the face that corresponds to $f \in \mathcal{F}$. If vertex index $i \in \mathcal{V}$ participates in face $f \in \mathcal{F}$, we denote the corresponding vertex index in $\overline{f} \in \overline{\mathcal{F}}$ as $i_{\overline{f}}$. The embeddings of the corresponding vertex are denoted as $\mathbf{x}_i$ (before deployment) and $\mathbf{y}_{i_{\overline{f}}}$ (after deployment). The reconfigurability can be defined as:

$$\mathbb{E}_{\text{reconfig}} = \sum_{f\in\mathcal{F}} \sum_{i,j\in f} w_{ij} \left(\|\mathbf{x}_i - \mathbf{x}_j\| - \left\|\mathbf{y}_{i_{\overline{f}}} - \mathbf{y}_{j_{\overline{f}}}\right\| \right)^2, \tag{3}$$

where $w_{ij} = \left(\frac{1}{2} \left(\|\mathbf{x}_i - \mathbf{x}_j\| + \left\|\mathbf{y}_{i_{\overline{f}}} - \mathbf{y}_{j_{\overline{f}}}\right\| \right) \right)^{-2}$ is the vertex-pair weight, recomputed at each iteration, which yields the squared relative edge-length error. The **planarity** energy $\mathbb{E}_{\text{planar}}$ encourages the polygonal faces to remain planar after deployment and is defined as:

$$\mathbb{E}_{\text{planar}}(\mathbf{Y}) = \sum_{\overline{f}\in\overline{\mathcal{F}}} \sum_{i,j\in\overline{f}} \left(\frac{(\mathbf{y}_j - \mathbf{y}_i)^\mathsf{T} \mathbf{n}_{\overline{f}}}{\|\mathbf{y}_j - \mathbf{y}_i\|} \right)^2, \tag{4}$$

where $\mathbf{n}_{\overline{f}}$ is the unit normal vector of the best-fit plane for each polygon face $\overline{f}$, which is recomputed at each iteration. The **shape approximation** term $\mathbb{E}_{\text{shape}}(\mathbf{Y} \mid \mathcal{M})$ quantifies how closely the deployed pattern $\mathbf{Y}$ matches the target surface $\mathcal{M}$:

$$\mathbb{E}_{\text{shape}}(\mathbf{Y} \mid \mathcal{M}) = \sum_{i=1}^{n} (\mathbf{y}_i - \mathbf{p}(\mathbf{y}_i))^\mathsf{T} \mathbf{n}_{\mathbf{p}}(\mathbf{y}_i). \tag{5}$$

Here, $\mathbf{p}(\mathbf{y}_i)$ denotes the point on the target surface closest to $\mathbf{y}_i$, and $\mathbf{n}_{\mathbf{p}}(\mathbf{y}_i)$ represents the normal at that point. Effectively, this term penalizes deviation by measuring the distance between each point and the tangent plane of its closest point on the target geometry $\mathcal{M}$. The **fairness** term $\mathbb{E}_{\text{fairness}}(\mathbf{Y}) = \|\mathbf{Y} - \mathbf{Y}^0\|_2^2$ encourages faces to stay close to their initial positions so the overall shape does not change drastically and retains a regular form (see Fig. 11 for an example). Here, $\mathbf{Y}^0$ is the initial embedding of $\mathbf{Y}$ obtained by directly lifting the deployed 2D pattern $\mathcal{T}^d$ onto the 3D shape $\mathcal{M}$ via parameterization. Specifically, we compute a parameterization for $\mathcal{M}$ by minimizing the symmetric Dirichlet energy [Smith and Schaefer 2015] to achieve low isometry distortion. This parameterization is used to lift the faces of the chosen pattern in its deployed configuration onto the target shape to obtain the initial 3D embedding $\mathbf{Y}^0$ to initialize $\mathbf{Y}$. See supplementary materials Sec. F for more details on implementation.

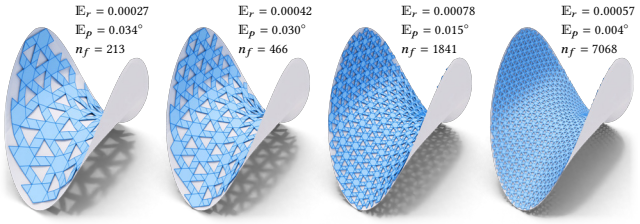

Fig. 12. Approximating the same target shape using varying numbers of tiles from the same pattern. Each example reports the number of faces (n_f), average unsquared reconfigurability error ($\mathbb{E}_r$), and average planarity error ($\mathbb{E}_p$) in degrees.

5 Results

Our theoretical insights enable the design of many previously unexplored tilings with deployable hinged kirigami structures, as shown in Fig. 13. Fabricated results using heavy-weight paper (Figures 10 and C.3) and felt (Fig. F.5) validate the accuracy of our simulated deployment process. We also conduct inverse design experiments:

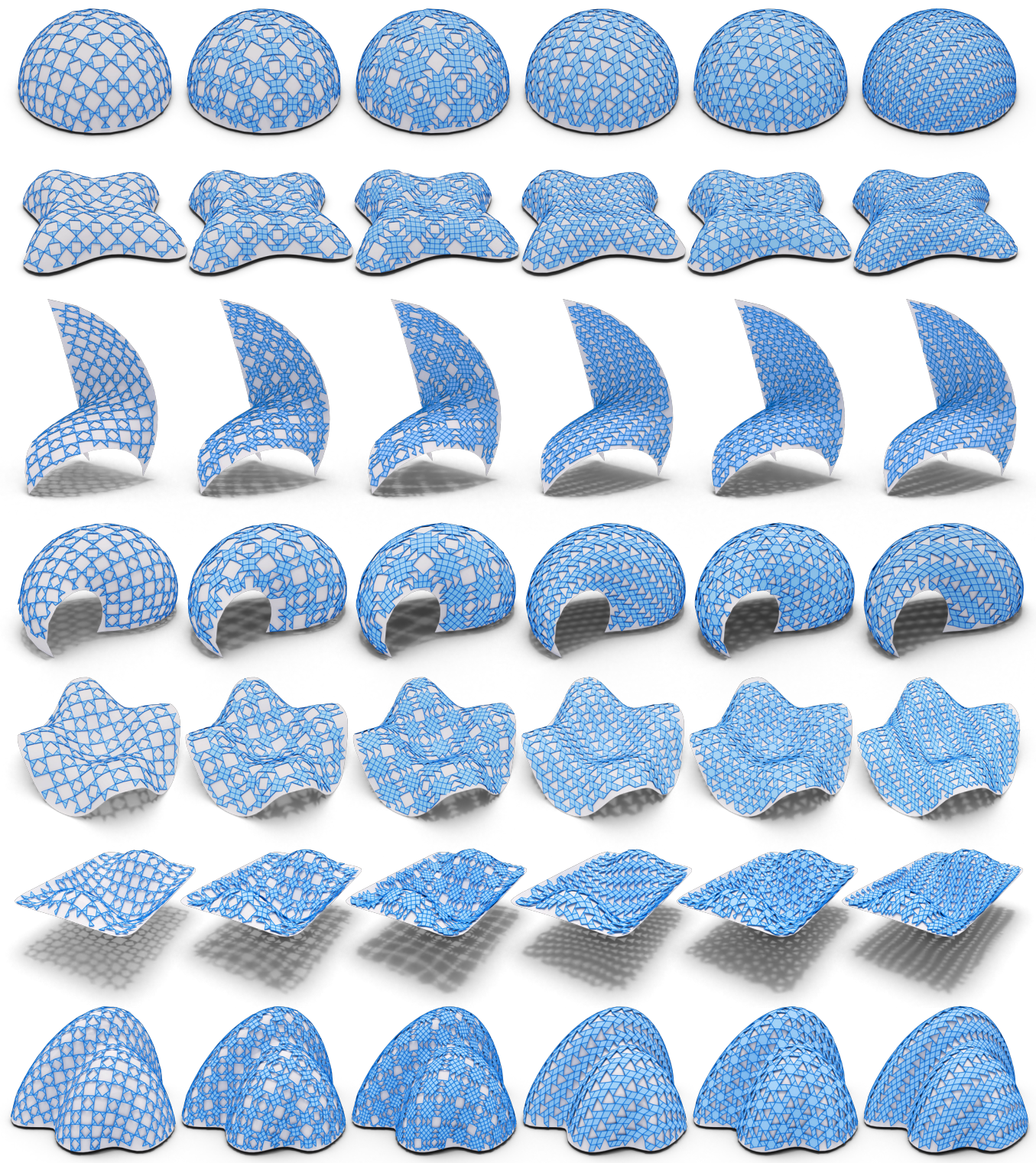

Fig. 13. Results with various tiling patterns applied to different 3D shapes. Deployed hinged kirigami tilings (blue) overlay the input surfaces (white, shadow casting disabled). The deployed tilings tightly fit the target shape, and we slightly offset the input shape along its normals for better visualization. In the supplementary materials Sec. F, we provide the optimized patterns before deployment, along with the statistics on shape complexity and optimization. All deployed hinged kirigami tilings exhibit a maximum reconfigurability error smaller than 10^{-2} and a maximum planarity error smaller than $0.1°$, ensuring fabricability.

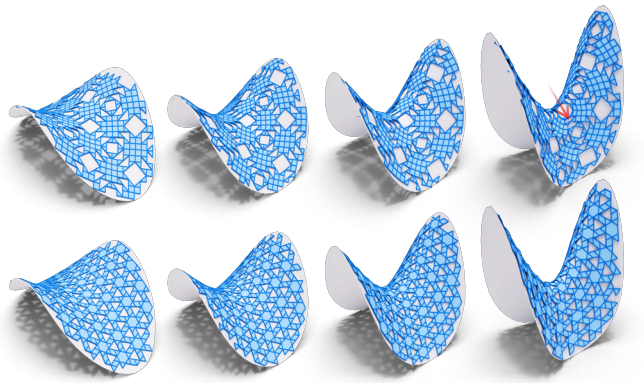

(a) Negative curvatures; each pattern consists of approximately 500 faces.

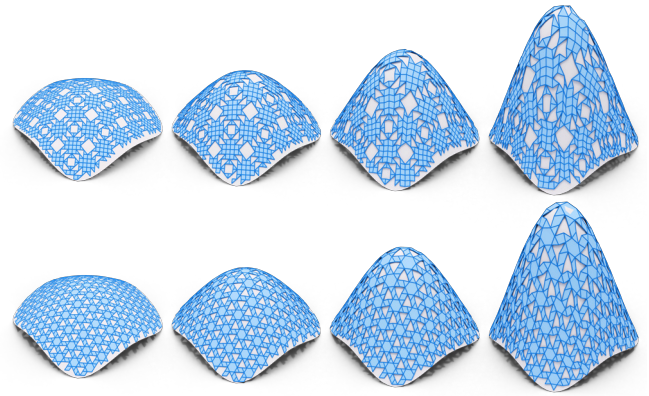

(b) Positive curvatures; each pattern consists of approximately 1000 faces.

Fig. 14. **Stress tests**: Using two distinct patterns to approximate similar shapes with increasing negative (a) and positive (b) curvature. The top-row pattern is more challenging to optimize than the bottom-row one due to having fewer holes to absorb distortion. This becomes particularly evident in extreme curvature cases, where irregularly shaped tiles appear (as highlighted by the red arrow), though all patterns remain deployable with maximum reconfigurability error smaller than 10^{-2} and maximum planarity error smaller than 0.1° (see full statistics in Supplemental Sec. F).

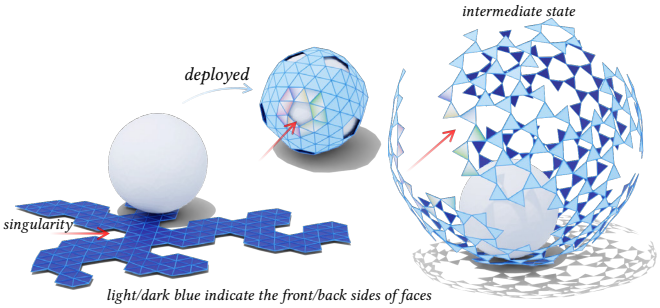

Fig. 15. Deploy a complete sphere shape from a flat tiling with singularities. The parameterization used for initialization is obtained by optimizing for a unit n-RoSy field using a similar approach to [Meekes and Vaxman 2021].

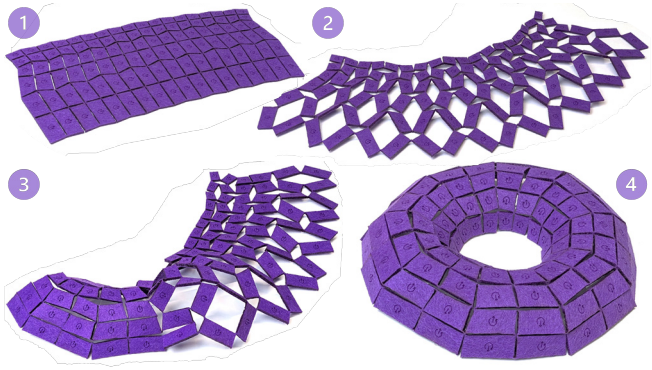

Fig. 16. A half torus (step ④) deployed from flat tiling (step ①), with two intermediate states shown in between, using felt material.

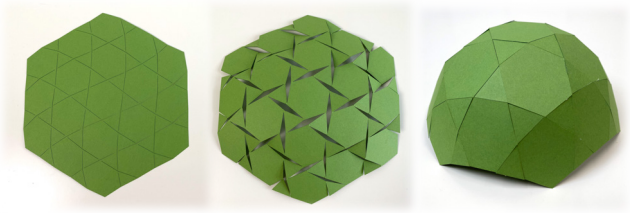

Fig. 17. A hemisphere shape deployed from hexagonal tilings, using paper.

given a chosen tiling (e.g., via our web UI) and a target 3D shape, users can specify different tiling densities (see Fig. 12). Our method then optimizes the 2D tiling geometry to ensure it can reconfigure and approximate the target shape. Fig. 13 shows results using 6 different tilings to approximate 7 shapes with prominent positive or negative curvatures. Fig. 14 shows a stress test, where two patterns are used to approximate shapes with increasing negative and positive curvatures. The formed holes after deployment effectively accommodate extreme curvatures, albeit at the cost of less regularity in the optimized tilings. Patterns with hole-free configurations at maximum opening angle, such as those in Fig. 2, are more structurally constrained. Achieving high curvature in such cases requires introducing singularities, as demonstrated in Fig. 15. Fabricating deployed 3D shapes from 2D tilings poses a tradeoff: thin joints cut into the tiling improve flexibility but are fragile and prone to breaking during rotation; thicker hinges offer durability but limit the achievable rotation angles. In preliminary experiments, we use a laser cutter on felt material, varying power settings to explore this balance. Figures 1,16-18 show fabrication results with the deployed shapes (secured with tape due to the bending resistance of hinges). Our inverse design framework enables a range of applications, including architecture (design Fig. 3), rapid deployment systems, and 3D puzzles Fig. 4. See supplementary materials and accompanying video for more implementation details and results. Code and web UI can be found at https://github.com/segaviv/kirigami_tessellations.

6 Conclusion, limitations & future work

Our work has several limitations that represent potential directions for future research. First, although certain non-manifold or non-periodic tilings can be cut open and reconfigured, they were not examined in this study. Establishing necessary and sufficient conditions for their deployability could significantly expand the design space for metamaterials, which we leave as future work.



Fig. 18. Photo of all fabricated results deployed from flat, hole-free tilings, constructed from paper or felt and secured with tape.

Second, our optimization focuses purely on geometric perspective–specifically, reconfigurability and planarity as deployment constraints. Material properties, actuation forces, stability analysis of the deployed structure and other mechanical factors were not considered. Our fabrication prototypes using felt or paper with partial cuts are preliminary; we observe that fabricated shapes with large holes or high negative curvatures (e.g., the light-blue and pink shapes shown in Fig. 18) exhibit reduced stability, necessitating boundary fixation to maintain their target shapes. Moreover, the partial-cut hinges in thick materials (such as felt) resist too much bending, and we believe that using more sophisticated mechanisms, such as those with prescribed rotation axes/paths, using pin joints or custom mechanical linkages, could offer greater reliability and control in deployment. Implementing such mechanical considerations and analyzing the stability of the deployed structure, considering the material properties and the hinge type, remains an open challenge.

Third, different tiling types exhibit distinct deployment characteristics, including varying degrees of conformal and shearing deformation. The holes in the pattern, along with the combinatorial permutations introduced during deployment, help absorb local distortions and enable curvature. In our current framework, the tiling type is provided as input rather than derived from the target geometry, and there is no guarantee that the target geometry can be realized from a given pattern. For example, physical fabrications show that a fully closed hemisphere shape can be achieved using a quad pattern (see Fig. 1) and hexagonal pattern (Fig. 17), but not with the triangular pattern (see Fig. F.4, *right*). Our current investigation of the realizable shape space associated with each pattern is largely empirical (Fig. 14); developing a mathematically rigorous framework for analyzing these shape spaces remains an open problem. Furthermore, automatically identifying optimal tiling types from geometric features, such as the curvature profile, is an interesting direction for future research, which could involve formulating a continuous model to analyze the behavior of the hinged kirigami structures. If such a model exists, one could gain a better understanding of the space of shapes that can be achieved from a given pattern, and where singularities could be placed to extend it.

Acknowledgments

The authors thank the anonymous reviewers for their valuable feedback. The authors are especially grateful to Helmut Pottmann for the discussions and his course offered at ETH Zurich during his stay with IGL. The authors thank Florian Rist and Danielle Luterbacher for their advice and assistance with fabrications. Special thanks to Ruben Wiersma for proofreading and for the professional rendering of Fig. 3. The authors further thank Mikhail Skopenkov and Alexander Bobenko for insightful comments on Definition 4.1. The authors thank all IGL members for their spiritual-academic support. This work was supported in part by the ERC Consolidator Grant No. 101003104 (MYCLOTH) and the Feodor Lynen Fellowship.

References

Ning An, August G Domel, Jinxiong Zhou, Ahmad Rafsanjani, and Katia Bertoldi. 2020. Programmable hierarchical kirigami. *Advanced Functional Materials* 30, 6 (2020), 1906711.

Hans-Jürgen Bandelt, Victor Chepoi, and David Eppstein. 2010. Combinatorics and Geometry of Finite and Infinite Squaregraphs. *SIAM Journal on Discrete Mathematics* 24, 4 (2010), 1399–1440. https://doi.org/10.1137/090760301

Quentin Becker, Uday Kusupati, Seiichi Suzuki, and Mark Pauly. 2024. Computational Design of a Kit of Parts for Bending Active Structures. *ACM Transactions on Graphics (TOG)* 43, 6 (2024), 1–16.

Quentin Becker, Seiichi Suzuki, Yingying Ren, Davide Pellis, Francis Julian Panetta, and Mark Pauly. 2023. C-shells: Deployable Gridshells with Curved Beams. *ACM Transactions on Graphics (TOG)* 42, 6 (2023), 1–17.

Alexandre Binninger, Floor Verhoeven, Philipp Herholz, and Olga Sorkine-Hornung. 2021. Developable Approximation via Gauss Image Thinning. *Computer Graphics Forum (proceedings of SGP 2021)* 40, 5 (2021), 289–300. https://doi.org/10.1111/cgf.14374

Sebastien JP Callens and Amir A Zadpoor. 2018. From flat sheets to curved geometries: Origami and kirigami approaches. *Materials Today* 21, 3 (2018), 241–264.

Toen Castle, Yigil Cho, Xingting Gong, Euiyeon Jung, Daniel M Sussman, Shu Yang, and Randall D Kamien. 2014. Making the cut: Lattice kirigami rules. *Physical review letters* 113, 24 (2014), 245502.

Toen Castle, Daniel M Sussman, Michael Tanis, and Randall D Kamien. 2016. Additive lattice kirigami. *Science advances* 2, 9 (2016), e1601258.

Paolo Celli, Connor McMahan, Brian Ramirez, Anton Bauhofer, Christina Naify, Douglas Hofmann, Basile Audoly, and Chiara Daraio. 2018. Shape-morphing architected sheets with non-periodic cut patterns. *Soft matter* 14, 48 (2018), 9744–9749.

Zekun Chang, Yuta Noma, Shuo Feng, Xinyi Yang, Kazuhiro Shinoda, Tung D Ta, Koji Yatani, Tomoyuki Yokota, Takao Someya, Yoshihiro Kawahara, et al. 2024. OriStitch: A Machine Embroidery Workflow to Turn Existing Fabrics into Self-Folding 3D Textiles. *arXiv preprint arXiv:2412.02891* (2024).

Ke Chen, Siqi Li, Peng Song, Jianmin Zheng, and Ligang Liu. 2024. mpcMech: Multi-Point Conjugation Mechanisms. *ACM Transactions on Graphics (TOG)* 43, 6 (2024), 1–14.

Tian Chen, Julian Panetta, Max Schnaubelt, and Mark Pauly. 2021. Bistable auxetic surface structures. *ACM Transactions on Graphics (TOG)* 40, 4 (2021), 1–9.

Xiang Chen, Changxi Zheng, Weiwei Xu, and Kun Zhou. 2014. An asymptotic numerical method for inverse elastic shape design. *ACM Transactions on Graphics (TOG)* 33, 4 (2014), 1–11.

Gary PT Choi, Levi H Dudte, and Lakshminarayanan Mahadevan. 2019. Programming shape using kirigami tessellations. *Nature materials* 18, 9 (2019), 999–1004.

Xiangxin Dang, Fan Feng, Huiling Duan, and Jianxiang Wang. 2021. Theorem for the design of deployable kirigami tessellations with different topologies. *Physical Review E* 104, 5 (2021), 055006.

Xiangxin Dang, Fan Feng, Huiling Duan, and Jianxiang Wang. 2022. Theorem on the compatibility of spherical kirigami tessellations. *Physical Review Letters* 128, 3 (2022).

Erik Demaine and Tomohiro Tachi. 2017. Origamizer: A practical algorithm for folding any polyhedron. In *33rd International Symposium on Computational Geometry (SoCG 2017)*. Dagstuhl Publishing, Saarbrucken/Wadern Germany, 34:1–34:16.

Levi H Dudte, Gary PT Choi, Kaitlyn P Becker, and L Mahadevan. 2023. An additive framework for kirigami design. *Nature Computational Science* 3, 5 (2023), 443–454.

Levi H Dudte, Etienne Vouga, Tomohiro Tachi, and Lakshminarayanan Mahadevan. 2016. Programming curvature using origami tessellations. *Nature materials* 15, 5 (2016), 583–588.

Michal Edelstein, Hila Peleg, Shachar Itzhaky, and Mirela Ben-Chen. 2022. Amigo: Computational design of amigurumi crochet patterns. In *Proceedings of the 7th Annual ACM Symposium on Computational Fabrication*. 1–11.

Yuanqing Gu, Zhibo Wei, Guowu Wei, Zhong You, Jiayao Ma, and Yan Chen. 2024. Kirigami-Inspired Three-Dimensional Metamaterials with Programmable Isotropic and Orthotropic Thermal Expansion. *Advanced Materials* 36, 50 (2024), 2411232.

Ruslan Guseinov, Eder Miguel, and Bernd Bickel. 2017. CurveUps: shaping objects from flat plates with tension-actuated curvature. *ACM Transactions on Graphics (TOG)* 36, 4 (2017), 64–1.

Siyuan He, Mengran Wu, Arthur Lebée, and Mélina Skouras. 2025. MatAIRials: Inflatable Metamaterials for Freefrom Surface Design. *Computer Graphics Forum (proceedings of SGP 2025)* 44, 5 (2025). https://doi.org/10.1111/cgf.70190

Ying He, Qing Fang, Zheng Zhang, Tielin Dai, Kang Wu, Ligang Liu, and Xiao-Ming Fu. 2024. Symmetric Piecewise Developable Approximations. *Computer Graphics Forum* 43, 7 (2024).

Alexandra Ion, Michael Rabinovich, Philipp Herholz, and Olga Sorkine-Hornung. 2020. Shape approximation by developable wrapping. *ACM Transactions on Graphics (TOG)* 39, 6 (2020), 1–12.

Alec Jacobson, Daniele Panozzo, et al. 2018. libigl: A simple C++ geometry processing library. https://libigl.github.io/.

Caigui Jiang, Dmitry Lyakhov, Florian Rist, Helmut Pottmann, and Johannes Wallner. 2024. Quad mesh mechanisms. *ACM Trans. Graph.* 43, 6, Article 243 (Nov. 2024), 17 pages. https://doi.org/10.1145/3687939

Caigui Jiang, Florian Rist, Helmut Pottmann, and Johannes Wallner. 2020. Freeform quad-based kirigami. *ACM Transactions on Graphics (TOG)* 39, 6 (2020), 1–11.

Caigui Jiang, Florian Rist, Hui Wang, Johannes Wallner, and Helmut Pottmann. 2022. Shape-morphing mechanical metamaterials. *Computer-Aided Design* 143 (2022), 103146.

Lishuai Jin, Antonio Elia Forte, Bolei Deng, Ahmad Rafsanjani, and Katia Bertoldi. 2020. Kirigami-inspired inflatables with programmable shapes. *Advanced Materials* 32, 33 (2020), 2001863.

David Jourdan, Pierre-Alexandre Hugron, Camille Schreck, Jonàs Martínez, and Sylvain Lefebvre. 2023. Shrink & Morph: 3D-printed self-shaping shells actuated by a shape memory effect. *ACM Transactions on Graphics (TOG)* 42, 6 (2023), 1–13.

David Jourdan, Mélina Skouras, Etienne Vouga, and Adrien Bousseau. 2020. Printing-on-fabric meta-material for self-shaping architectural models. In *Advances in Architectural Geometry 2020*. Les Presses des ponts, Paris, France, 14:1–14:19.

David Jourdan, Mélina Skouras, Etienne Vouga, and Adrien Bousseau. 2022. Computational Design of Self-Actuated Surfaces by Printing Plastic Ribbons on Stretched Fabric. In *Computer Graphics Forum*, Vol. 41. Wiley Online Library, 493–506.

Martin Kilian, Aron Monszpart, and Niloy J. Mitra. 2017. String Actuated Curved Folded Surfaces. *ACM Transactions on Graphics (TOG)* 36, 4 (July 2017), 13. https://doi.org/10.1145/3072959.3015460

Mattis Koh, Yue Wang, Kristina Shea, and Tian Chen. 2023. Shape reconfiguring bistable structures using heat activated fibers. *Engineering Structures* 295 (2023), 116792.

Mina Konaković, Keenan Crane, Bailin Deng, Sofien Bouaziz, Daniel Piker, and Mark Pauly. 2016. Beyond Developable: Computational Design and Fabrication with Auxetic Materials. *ACM Transactions on Graphics (TOG)* 35, 4, Article 89 (2016), 11 pages. https://doi.org/10.1145/2897824.2925944

Mina Konaković, Julian Panetta, Keenan Crane, and Mark Pauly. 2018. Rapid Deployment of Curved Surfaces via Programmable Auxetics. *ACM Transactions on Graphics (TOG)* 37, 4, Article 106 (2018), 13 pages. https://doi.org/10.1145/3197517.3201373

Uday Kusupati, Florin Isvoranu, Seiichi Suzuki, and Mark Pauly. 2023. RUM: Reconfigurable Umbrella Mesh. *Advances in Architectural Geometry 2023* (2023), 474.

Jae-Hwang Lee, Jonathan P Singer, and Edwin L Thomas. 2012. Micro-/nanostructured mechanical metamaterials. *Advanced materials* 24, 36 (2012), 4782–4810.

Daoming Liu, Davide Pellis, Yu-Chou Chiang, Florian Rist, Johannes Wallner, and Helmut Pottmann. 2023. Deployable strip structures. *ACM Transactions on Graphics (TOG)* 42, 4 (2023), 103:1–103:16.

Weiqi Liu, Song Cao, and Yan Chen. 2024. Mountain-valley crease reconfiguration of 4-crease origami vertices and tessellations. *International Journal of Mechanical Sciences* 273 (2024), 109224. https://doi.org/10.1016/j.ijmecsci.2024.109224

Jiayao Ma, Jichao Song, and Yan Chen. 2018. An origami-inspired structure with graded stiffness. *International Journal of Mechanical Sciences* 136 (2018), 134–142.

Luigi Malomo, Jesús Pérez, Emmanuel Iarussi, Nico Pietroni, Eder Miguel, Paolo Cignoni, and Bernd Bickel. 2018. FlexMaps: computational design of flat flexible shells for shaping 3D objects. *ACM Transactions on Graphics (TOG)* 37, 6 (2018), 1–14.

Merel Meekes and Amir Vaxman. 2021. Unconventional patterns on surfaces. *ACM Transactions on Graphics (TOG)* 40, 4 (2021), 1–16.

Vidya Narayanan, Lea Albaugh, Jessica Hodgins, Stelian Coros, and James Mccann. 2018. Automatic machine knitting of 3D meshes. *ACM Transactions on Graphics (TOG)* 37, 3 (2018), 1–15.

Koya Narumi, Kazuki Koyama, Kai Suto, Yuta Noma, Hiroki Sato, Tomohiro Tachi, Masaaki Sugimoto, Takeo Igarashi, and Yoshihiro Kawahara. 2023. Inkjet 4D print: Self-folding tessellated origami objects by inkjet UV printing. *ACM Transactions on Graphics (TOG)* 42, 4 (2023), 1–13.

Fuki Ono, Haruto Kamijo, Miwako Kase, Seri Nishimoto, Kotaro Sempuku, Mizuki Shigematsu, and Tomohiro Tachi. 2024. Growth-induced transformable surfaces realized by bending-active scissors grid. *Architectural Intelligence* 3, 1 (2024), 21.

Julian Panetta, Florin Isvoranu, Tian Chen, Emmanuel Siéfert, Benoît Roman, and Mark Pauly. 2021. Computational inverse design of surface-based inflatables. *ACM Transactions on Graphics (TOG)* 40, 4 (2021), 1–14.

Julian Panetta, Mina Konaković-Luković, Florin Isvoranu, Etienne Bouleau, and Mark Pauly. 2019. X-shells: A new class of deployable beam structures. *ACM Transactions on Graphics (TOG)* 38, 4 (2019), 1–15.

Jesús Pérez, Miguel A Otaduy, and Bernhard Thomaszewski. 2017. Computational design and automated fabrication of Kirchhoff-Plateau surfaces. *ACM Transactions on Graphics (TOG)* 36, 4 (2017), 1–12.

Jesús Pérez, Bernhard Thomaszewski, Stelian Coros, Bernd Bickel, José A Canabal, Robert Sumner, and Miguel A Otaduy. 2015. Design and fabrication of flexible rod meshes. *ACM Transactions on Graphics (TOG)* 34, 4 (2015), 1–12.

Ahmad Rafsanjani and Katia Bertoldi. 2017. Buckling-induced kirigami. *Physical review letters* 118, 8 (2017), 084301.

Ahmad Rafsanjani and Damiano Pasini. 2016. Bistable auxetic mechanical metamaterials inspired by ancient geometric motifs. *Extreme Mechanics Letters* 9 (2016), 291–296.

Jing Ren, Aviv Segall, and Olga Sorkine-Hornung. 2024b. Digital 3D Smocking Design. *ACM Transactions on Graphics (TOG)* 43, 2 (2024), 14:1–14:17.

Yingying Ren, Uday Kusupati, Julian Panetta, Florin Isvoranu, Davide Pellis, Tian Chen, and Mark Pauly. 2022. Umbrella Meshes: Elastic Mechanisms for Freeform Shape Deployment. *ACM Transactions on Graphics (TOG)* 41, 4 (2022), 1–15.

Yingying Ren, Julian Panetta, Tian Chen, Florin Isvoranu, Samuel Poincloux, Christopher Brandt, Alison Martin, and Mark Pauly. 2021. 3D weaving with curved ribbons. *ACM Transactions on Graphics (TOG)* 40, 4 (2021), 127:1–127:15.

Yingying Ren, Julian Panetta, Seiichi Suzuki, Uday Kusupati, Florin Isvoranu, and Mark Pauly. 2024a. Computational homogenization for inverse design of surface-based inflatables. *ACM Transactions on Graphics (TOG)* 43, 4 (2024), 1–18.

Mark Schenk and Simon D Guest. 2013. Geometry of Miura-folded metamaterials. *Proceedings of the National Academy of Sciences* 110, 9 (2013), 3276–3281.

Jonas Schikore, Eike Schling, Thomas Oberbichler, and Anna Bauer. 2021. Kinetics and design of semi-compliant grid mechanisms. In *Advances in Architectural Geometry Conference (AAG 2020)*. Paris, France.

Aviv Segall, Jing Ren, Amir Vaxman, and Olga Sorkine-Hornung. 2024. Fabric Tessellation: Realizing Freeform Surfaces by Smocking. *ACM Transactions on Graphics (TOG)* 43, 4 (2024), 1–20.

Nicholas Sharp et al. 2019. Polyscope. www.polyscope.run.

Yuta Shimoda, Kai Suto, Sei Hayashi, Tomoyuki Gondo, and Tomohiro Tachi. 2023. Developable Membrane Tensegrity Structures Based on Origami Tessellations. *Advances in Architectural Geometry 2023* (2023), 303.

Mélina Skouras, Bernhard Thomaszewski, Peter Kaufmann, Akash Garg, Bernd Bickel, Eitan Grinspun, and Markus Gross. 2014. Designing inflatable structures. *ACM Transactions on Graphics (TOG)* 33, 4 (2014), 1–10.

Jason Smith and Scott Schaefer. 2015. Bijective parameterization with free boundaries. *ACM Transactions on Graphics (TOG)* 34, 4 (2015), 1–9.

Oded Stein, Eitan Grinspun, and Keenan Crane. 2018. Developability of triangle meshes. *ACM Transactions on Graphics (TOG)* 37, 4 (2018), 1–14.

Tomohiro Tachi. 2008. Origamizer. https://origami.c.u-tokyo.ac.jp/~tachi/software/index.html

Tomohiro Tachi. 2013. Designing Freeform Origami Tessellations by Generalizing Resch's Patterns. *Journal of Mechanical Design* 135, 11 (10 2013), 111006:1–111006:10. https://doi.org/10.1115/1.4025389

Yichao Tang, Yanbin Li, Yaoye Hong, Shu Yang, and Jie Yin. 2019. Programmable active kirigami metasheets with more freedom of actuation. *Proceedings of the National Academy of Sciences* 116, 52 (2019), 26407–26413.

Yichao Tang and Jie Yin. 2017. Design of cut unit geometry in hierarchical kirigami-based auxetic metamaterials for high stretchability and compressibility. *Extreme Mechanics Letters* 12 (2017), 77–85.

Andreas Walker and Kristina Shea. 2024. Computational design of 4D printed shape morphing lattices undergoing large deformation. *Smart Materials and Structures* 33, 11 (2024), 115047.

Fei Wang, Xiaogang Guo, Jingxian Xu, Yihui Zhang, and CQ Chen. 2017. Patterning curved three-dimensional structures with programmable kirigami designs. *Journal of Applied Mechanics* 84, 6 (2017), 1–7.

Zhiyan Y Wei, Zengcai V Guo, Levi Dudte, Haiyi Y Liang, and Lakshminarayanan Mahadevan. 2013. Geometric mechanics of periodic pleated origami. *Physical review letters* 110, 21 (2013), 215501.

Kui Wu, Hannah Swan, and Cem Yuksel. 2019. Knittable Stitch Meshes. *ACM Transactions on Graphics (TOG)* 38, 1 (2019), 1–13.

Yi Yang, Marcelo A Dias, and Douglas P Holmes. 2018. Multistable kirigami for tunable architected materials. *Physical Review Materials* 2, 11 (2018), 110601.

Xiaoting Zhang, Guoxin Fang, Melina Skouras, Gwenda Gieseler, Charlie C.L. Wang, and Emily Whiting. 2019. Computational Design of Fabric Formwork. *ACM Transactions on Graphics (TOG)* 38, 4 (2019), 109:1–109:13.

Zheng-Yu Zhao, Qing Fang, Wenqing Ouyang, Zheng Zhang, Ligang Liu, and Xiao-Ming Fu. 2022. Developability-driven piecewise approximations for triangular meshes. *ACM Transactions on Graphics (TOG)* 41, 4 (2022), 1–13.

Supplemental Materials

A Cutting tilings into hinged kirigami structure

Given a planar tiling $\mathcal{T} = (\mathcal{V}, \mathcal{F})$, where all vertices have even valency, our goal is to construct a complete cut $\mathcal{E}_c$ that covers all interior edges in $\mathcal{T}$, such that applying $\mathcal{E}_c$ to $\mathcal{T}$ yields a hinged kirigami structure $\overline{\mathcal{T}} = (\overline{\mathcal{V}}, \overline{\mathcal{F}})$, in which every vertex in $\overline{\mathcal{V}}$ is shared by exactly two faces.

The construction is conceptually simple. Consider a vertex $v \in \mathcal{V}$ with valency $2k$. Let its incident (undirected) edges be cyclically ordered as $e_1, e_2, \cdots, e_{2k}$, where each pair of consecutive edges e_i, e_{i+1} (indices modulo $2k$) belongs to the same face. Let v_i be the other vertex of edge $e_i, \forall i = 1, \cdots, 2k$. To satisfy the hinged condition, i.e., each vertex is shared by exactly two faces, the directed cuts at v must alternate in direction (or follow a consistent reversal):

$$(v_1 \to v), (v \to v_2), (v_3 \to v), \cdots, (v_{2k-1} \to v), (v \to v_{2k}) \quad \text{(A.1)}$$

No two consecutive edge cuts may point in the same direction (both into or out of v), otherwise v would either belong to only one face in the resulting kirigami or be shared by more than two–both situations violating the definition of a valid hinged kirigami structure (see Fig. 7 in the main paper). Thus, to construct a valid complete cut $\mathcal{E}_c$ for $\mathcal{T}$, we ensure that each interior vertex respects the alternating pattern in Eq. (A.1), and that every interior edge is included exactly once in $\mathcal{E}_c$. This can be achieved via breadth-first or depth-first search, see Fig. A.1 for an example. Specifically, we propagate edge directions starting from a seed edge, ensuring alternation at every visited vertex. Since we assume $\mathcal{T}$ is a planar orientable manifold and all interior vertices have even valency, its faces $\mathcal{F}$ are guaranteed to be two-colorable. Once face colors are assigned, we extract the cut edge directions from the edge orientations of the faces with the same color (say, pink shown in Fig. A.1) to form $\mathcal{E}_c$. Algorithm 1 provides the pseudocode for face coloring and constructing $\mathcal{E}_c$. Algorithm 2 shows how to apply the complete cut to generate the hinged kirigami structure $\overline{\mathcal{T}}$, where duplicated vertices and edges are created along $\mathcal{E}_c$, preserving face geometry but updating vertex indices.

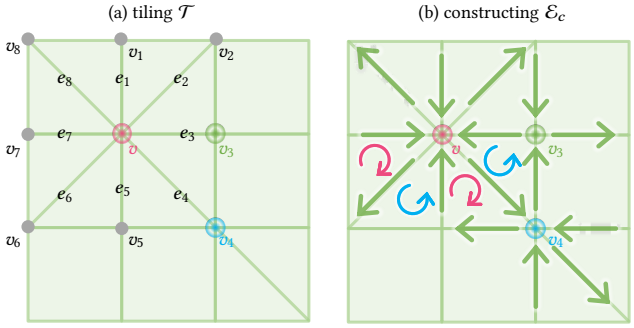

Fig. A.1. (a) The highlighted vertex v has valency $2k$ (here, $k = 4$), with incident edges cyclically ordered as $e_i = (v, v_i)$ for $i = 1, \ldots, 2k$. In any valid complete cut $\mathcal{E}_c$, the directions of two consecutive cut edges must alternate, as shown by green arrows in (b). To construct such an alternating complete cut, we propagate directions from a seed edge. Starting with $\mathcal{E}_c = \emptyset$, we add $(v_1 \to v)$, then alternate around v: $(v \to v_2), (v_3 \to v), \ldots, (v \to v_8)$. Moving to v_3, where one incident edge is already directed, we continue the alternating pattern. This process iteratively builds $\mathcal{E}_c$ by visiting all interior edges. It is equivalent to 2-coloring the faces with pink and blue (no adjacent faces share a color) and then assigning clockwise/counterclockwise directions to pink/blue, as shown in (b).

B Uniformly deployable tilings

In this section, we prove the necessary and sufficient condition for a uniformly deployable tiling by construction, as stated in Proposition 4.1. For clarity, we restate it below:

Proposition (necessary and sufficient condition for uniform deployability). For a planar tiling with all interior vertices of even valency, the following are equivalent: (1) Every interior vertex in the tiling is deployment-friendly. (2) The resulting hinged kirigami structure is uniformly deployable in 2D.

Proof. We first show (2) $\Rightarrow$ (1), i.e., if a planar tiling where all interior vertices have even valency is uniformly deployable (see Definition 3.1), then every interior vertex in the tiling must be deployment-friendly (see Definition 4.1).

ALGORITHM 1: Constructing complete cut $\mathcal{E}_c$

Input: tiling $\mathcal{T} = (\mathcal{V}, \mathcal{F})$ with even valency at all int. vertices
Output: complete cut $\mathcal{E}_c$ as a set of directed edges

$\mathcal{E}_c \leftarrow \emptyset, Q \leftarrow \emptyset$
pick arbitrary face f, assign $c_f \leftarrow 0$, enqueue f into Q
while Q not empty **do**
  $f \leftarrow \text{dequeue}(Q)$
  for all uncolored neighbors f' of f **do**
    $c_{f'} \leftarrow 1 - c_f$, enqueue f' into Q
  end for
end while
for all $f \in \mathcal{F}$ with $c_f = 0$ **do**
  let $f = (v_0, \ldots, v_{p-1})$ counterclockwise
  for $i = 0$ to $p - 1$ **do**
    add $(v_i \to v_{i+1 \bmod p})$ to $\mathcal{E}_c$
  end for
end for
return $\mathcal{E}_c$

ALGORITHM 2: Cut tiling into hinged kirigami structure

Input: tiling $\mathcal{T} = (\mathcal{V}, \mathcal{F})$ with a complete cut $\mathcal{E}_c$
Output: a hinged kirigami structure $\overline{\mathcal{T}} = (\overline{\mathcal{V}}, \overline{\mathcal{F}})$

initialize $\overline{\mathcal{V}} \leftarrow \mathcal{V}, \overline{\mathcal{F}} \leftarrow \mathcal{F}$
build half-edge structure of $\mathcal{T}$
for all directed edge $e = (v_i \to v_j) \in \mathcal{E}_c$ **do**
  create new vertex $\overline{v}_j \leftarrow$ duplicate of v_j
  add $\overline{v}_j$ to $\overline{\mathcal{V}}$
  replace v_j with $\overline{v}_j$ in the face f containing the edge e
  if the edge e_{next} in f with origin v_j is not a boundary edge **then**
    replace v_j with $\overline{v}_j$ in the twin face of e_{next}
  end if
end for
return $\overline{\mathcal{T}} = (\overline{\mathcal{V}}, \overline{\mathcal{F}})$

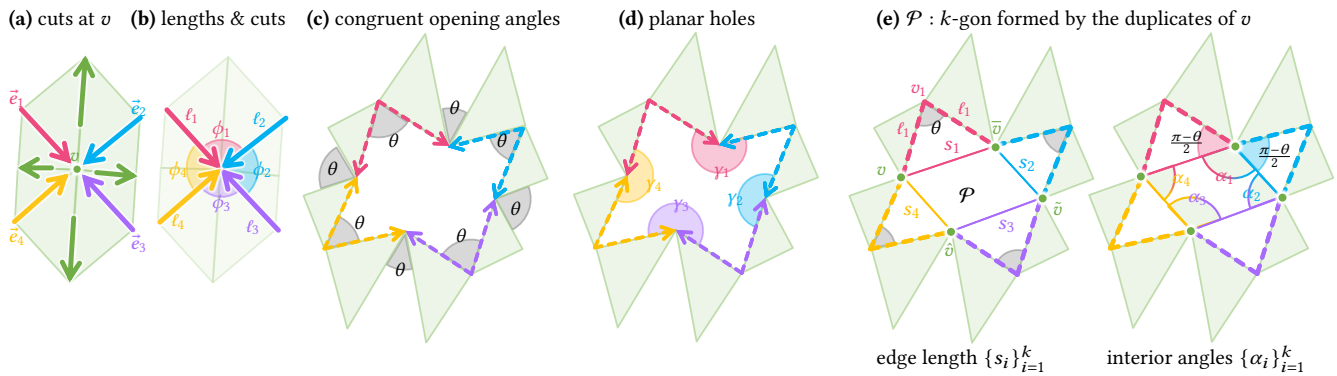

Fig. B.2. **Notations** used in the proof presented in Sec. B. (a) The cut edges ending at vertex v are denoted $\vec{e}_1, \cdots, \vec{e}_k$ (in this example $k = 4$). (b) Let ℓ_i be the length of $\vec{e}_i$ and ϕ_i the angle between consecutive cut edges. (c) Assuming uniform deployability, all opening angles between the duplicated edges are equal (colored in gray), denoted as θ. (d) If the tiling deploys in 2D, the emerging holes from cutting are planar $2k$-gons. (e) Connecting all duplicates of the same vertex (in this case $v, \overline{v}, \tilde{v}, \hat{v}$) forms a planar k-gon whose edge lengths $\{s_i\}$ and interior angles $\{\alpha_i\}$ can be directly computed.

Consider an interior vertex v with valency $2k$. As discussed in Sec. A, a valid complete cut requires exactly k cuts directed into v. Let these incoming edges, ordered cyclically around v, be $\vec{e}_1, \cdots, \vec{e}_k$, and let v_i denote the starting vertex of cut edge $\vec{e}_i$. See Fig. B.2 (a). We denote the length of $\vec{e}_i$ as ℓ_i and the angle between $(\vec{e}_i, \vec{e}_{i+1})$, index modulo k, as ϕ_i. See Fig. B.2 (b). Since we assume the tiling to be a planar manifold without holes or gaps, we know:

$$\sum_{i=1}^{k} \phi_i = 2\pi. \tag{B.2}$$

Since we assume the tiling is uniformly deployable, all the opening angles between duplicated edges are equal, denoted as θ. See Fig. B.2 (c), where duplicated edges are shown in matching colors. By assumption, the tiling is deployable in 2D, so all faces remain rigid: their angles and edge lengths are preserved throughout the motion, and any openings (holes) that emerge during deployment remain planar. Thus, we can compute the interior angles for the emerging holes γ_i, as illustrated in Fig. B.2 (d):

$$\gamma_i = 2\pi - \phi_i - \theta, \ i = 1 \cdots k. \tag{B.3}$$

Now, consider the triangular hole formed by a pair of duplicated edges induced by the cut, e.g. $v_1 \rightarrow v$, which produces a duplicated vertex $\overline{v}$, as shown in Fig. B.2 (e). The points $v_1, v, \overline{v}$ form an isosceles triangle: given the opening angle θ and cut length ℓ_1, the distance between v and $\overline{v}$ can be computed as:

$$s_1 = 2\ell_1 \sin\tfrac{\theta}{2}. \tag{B.4}$$

This generalizes to all incident cuts. Let $\mathcal{P}$ be the k-gon formed by the k duplicates of v after applying all incident cuts around v. See Fig. B.2 (f) for an illustration. The *edge lengths* $\{s_i\}_{i=1}^k$ of $\mathcal{P}$ are:

$$s_i = 2\ell_i \sin\tfrac{\theta}{2}, \ i = 1 \cdots k. \tag{B.5}$$

We can also determine the interior angles $\{\alpha_i\}_{i=1}^k$ of $\mathcal{P}$:

$$\alpha_i = \gamma_i - (\pi - \theta) = \pi - \phi_i. \tag{B.6}$$

We can easily check that $\sum_{i=1}^k \alpha_i = k\pi - \sum_{i=1}^k \phi = (k-2)\pi$. That is, $\mathcal{P}$ is a valid k-gon by construction with edge lengths $\{2\ell_i \sin\frac{\theta}{2}\}$ and interior angles $\{\pi - \phi_i\}$. Scaling $\mathcal{P}$ down uniformly by a factor of $2\sin\frac{\theta}{2}$ yields a valid k-gon, denoted as $\mathcal{P}'$, with edge lengths $\{\ell_i\}$ and the same interior angles $\{\pi - \phi_i\}$. Note that $\mathcal{P}'$ is equivalent to the polygon formed by translating the cut edges $\vec{e}_1, \cdots, \vec{e}_k$ and connecting the ending point of $\vec{e}_{i+1}$ to the starting point of $\vec{e}_i$. Since we know that $\mathcal{P}'$ is planar, we can conclude that $\sum_{i=1}^k \vec{e}_i = \vec{0}$. By definition, this confirms that v is deployment-friendly. Since the choice of v was arbitrary, it follows that every vertex in a uniformly deployable tiling is deployment-friendly.

To show that (1) $\Rightarrow$ (2), we apply similar reasoning: given the edge lengths and interior angles, the shape of the polygon formed by duplicated vertices is uniquely determined. If a vertex is deployment-friendly, then the construction guarantees that the opening angles between duplicated edges are congruent. Therefore, all hinges on such vertices open uniformly, and the tiling is uniformly deployable. □

In the special case where a vertex v has valency 4, there are exactly two cuts incident to v, that is, $k = 2$ in the analysis above. Let the lengths of these two cuts be ℓ_1 and ℓ_2 and let the angles between them be ϕ_1 and ϕ_2, which satisfy $\phi_1 + \phi_2 = 2\pi$. For v to be deployment-friendly, we must be able to construct a 2-gon with edge lengths ℓ_1 and ℓ_2 and interior angles ϕ_1 and ϕ_2. A 2-gon in this context is a degenerate polygon—a straight segment—formed by $v_1 \rightarrow v_2 \rightarrow v_1$, closing back on itself. To satisfy the geometric constraints of a valid 2-gon, it must hold that $\ell_1 = \ell_2$ and $\phi_1 = \phi_2 = \pi$. In other words, for a 4-valent vertex to be deployment-friendly, the two cuts passing through it must be collinear and of equal length.

Lemma B.1. For a tiling composed of 4-valent interior vertices, the following statements are equivalent: (1) For every interior vertex v, the two incident cuts are collinear and of equal length. (2) The tiling is uniformly deployable in 2D.

For such a uniformly deployable tiling, the holes created during deployment take on a diamond shape, since each hole is formed by two pairs of duplicated edges that originally have equal length. It is known that a diamond with fixed edge lengths achieves its maximum area when it becomes a square. This geometric fact is leveraged in [Jiang et al. 2020] to formulate the maximal area expansion configuration. This lemma also explains why the tiling in Fig. 8 of the main paper is not uniformly deployable: the cuts at the valency-4 vertices are not collinear.

ALGORITHM 3: Identify unit tile from parallel line families

Input: $\mathcal{L} = \{\ell_i\}$, each family $\ell_i \in \mathcal{L}$ with unit directional vectors $\mathbf{t}_i$, unit normals $\mathbf{n}_i$, and shifts d_i
Output: Periodicity (λ_1, λ_2)

$\lambda_1 \leftarrow \frac{d_2}{\mathbf{t}_1^\mathsf{T}\mathbf{n}_2}, \lambda_2 \leftarrow \frac{d_1}{\mathbf{t}_2^\mathsf{T}\mathbf{n}_1}$
for $i \leftarrow 3$ **to** $|\mathcal{L}|$ **do**
  $\lambda \leftarrow \frac{d_i}{\mathbf{t}_1^\mathsf{T}\mathbf{n}_i}$
  find the smallest integers n, m s.t. $n\lambda = m\lambda_1$
  $\lambda_1 \leftarrow m\lambda_1$
  $\lambda \leftarrow \frac{d_i}{\mathbf{t}_2^\mathsf{T}\mathbf{n}_i}$
  find the smallest integers n, m s.t. $n\lambda = m\lambda_2$
  $\lambda_2 \leftarrow m\lambda_2$
end for
return (λ_1, λ_2)

C Non-uniformly deployable tilings

Proposition 4.1 and the discussion in Sec. B focus on uniformly deployable tilings, which can be verified by checking whether every vertex is deployment-friendly. For a tiling that contains deployment-unfriendly vertices, as shown in Fig. 10 of the main paper and Fig. C.3, Proposition 4.1 tells us only that it cannot be deployed uniformly, meaning the opening angles cannot all be congruent. However, such a tiling may still be deployable. In this case, the opening angles between duplicated edges may differ, but they remain *mutually dependent* due to the global connectivity of the hinged kirigami structure. To determine deployability, we must optimize for the opening angles. For the hinged kirigami structure $\overline{\mathcal{T}} = (\overline{\mathcal{V}}, \overline{\mathcal{F}})$ derived from the original tiling $\mathcal{T}$, we select a random seed edge e and attempt to compute a valid embedding of $\overline{\mathcal{V}}$ when the opening angle $\theta(e)$ is set to a predefined value. We formulate an optimization problem with the following objectives: (1) Faces remain rigid; (2) The specified opening angle $\theta(e)$ is enforced; (3) The deployed configuration preserves the periodicity of the original tiling. If a valid solution is found, we say the tiling is deployable. For inverse design, we focus exclusively on uniformly deployable tilings, as their deployment depends on a single parameter (the opening angle) and admits explicit construction without the need for optimization.

D Extracting the unit tile from parallel line families

Given a set of distinct parallel line families $\mathcal{L} = \{\ell_i\}$, each family $\ell_i = (\mathbf{p}_i, \mathbf{q}_i, d_i)$ is parameterized by:

- A baseline $\ell_i(0)$ passing through two distinct points $\mathbf{p}_i$ and $\mathbf{q}_i$;
- Parallel replicas $\ell_i(m), m \in \mathbb{Z}$, generated by translating $\ell_i(0)$ along its normal direction: $\ell_i(m) = \{\mathbf{x} \in \mathbb{R}^2 \mid \mathbf{x} = \mathbf{x}_0 + md_i\mathbf{n}_i, \forall \mathbf{x}_0 \in \ell_i(0)\}$, where the unit normal $\mathbf{n}_i$ is orthogonal to the unit direction vector $\mathbf{t}_i = (\mathbf{q_i} - \mathbf{p}_i)/\|\mathbf{q_i} - \mathbf{p}_i\|$.

We assume the first two families of parallel lines are not parallel to each other, i.e., $\mathbf{t}_1 \nparallel \mathbf{t}_2$. The unit tile of this multi-line grid $\mathcal{L}$ is the smallest parallelogram spanned by vectors $\mathbf{u}_1 = \lambda_1\mathbf{t}_1$ and $\mathbf{u}_2 = \lambda_2\mathbf{t}_2$ such that translations by $(\mathbf{u}_1, \mathbf{u}_2)$ preserve all line intersections within $\mathcal{L}$. Formally, we seek the smallest values of λ_1, λ_2 ensuring that for every pair $\ell_i, \ell_j \in \mathcal{L}$ and for all integers $m, n, a, b \in \mathbb{Z}$, there exist integers $c, d \in \mathbb{Z}$ such that:

$$\mathbf{x}_{ij}(c, d) = \mathbf{x}_{ij}(a, b) + m\lambda_1\mathbf{t}_1 + n\lambda_2\mathbf{t}_2, \tag{D.7}$$

where $\mathbf{x}_{ij}(a, b) := \ell_i(a) \cap \ell_j(b)$ denotes the intersection between the a-th replica of ℓ_i and the b-th replica of ℓ_j. Informally, starting from any intersection of ℓ_i and ℓ_j, one can reach another intersection by translating in integer steps along the directions $\lambda t_1, \lambda t_2$. We determine the values of (λ_1, λ_2) using Algorithm 3. Essentially, we scale the unit tile by ℓ_1 and ℓ_2 to fit the remaining families.

E Implementation

The tiling generation UI is web-based, and the inverse design algorithm is implemented in C++ using the libraries libigl [Jacobson et al. 2018] and Polyscope [Sharp et al. 2019]. We also implemented a simulation for deploying an optimized tiling into the target shape. Interpolated intermediate positions are used as initialization, then optimized for reconfigurability, planarity, and smoothness across deployment states. All experiments are carried out on an Apple M1 Max chip and 32 GB memory. For the inverse design, the embedding $\mathbf{X}$ (the 2D layout before embedding) is initialized using the vertex positions from the initial tiling $\mathcal{T}$. The embedding $\mathbf{Y}$ (the 3D configuration after deployment) is initialized by lifting the deployed pattern $\mathcal{T}^d$ onto the target shape $\mathcal{M}$ using low-distortion (minimizing the symmetric Dirichlet energy) parameterization [Smith and Schaefer 2015]. This initialization is also used in the fairness energy term $\mathbb{E}_{\text{fairness}}$. For all experiments, we use the same parameters: $\omega_1 = 10, \omega_2 = 10, \omega_3 = 0.1, \omega_4 = 0.5$. During the optimization, we gradually decrease the weight of the fairness energy ω_4 to allow the deployed configuration to slide on the target mesh, thereby improving reconfigurability and planarity errors. We find that the planarity term is essential: without it, $\mathbb{E}_{\text{reconfig}}$ is prone to getting stuck in local minima. Optimization is performed using Newton's method and terminates when the maximum reconfigurability error for any face falls below 10^{-2} and the maximum planarity error is less than $0.1°$. In most experiments, convergence is reached within a few seconds.

F Additional results

Fig. F.4 shows two examples of failure cases. Compared to patterns that contain holes in the deployed state (e.g., in Fig. 13), fully closed patterns make it more difficult to achieve high curvatures while maintaining reasonable fabrication or shape approximation error. In such cases, introducing singularities is necessary (see Fig. 15 for an example). As shown in Fig. 1, Fig. 2 and Fig. 17, a hemispherical shape can be successfully realized using the quad pattern and the hexagonal pattern, whereas the triangular pattern in Fig. F.4 (*right*) performs poorly. This suggests that the shape spaces of different patterns vary and require further investigation.

Figures F.5 and F.6 show additional deployment process of under-explored tilings. Fig. F.7 shows the optimized planar tilings corresponding to the results in Fig. 13, prior to deployment. Table F.1 and Table F.2 report the shape complexity and runtime of experiments shown in the main paper.

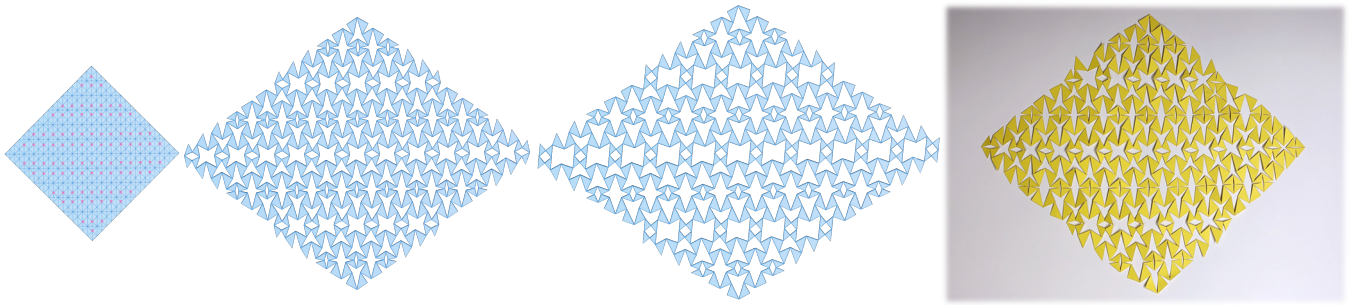

Fig. C.3. This tiling contains deployment-unfriendly vertices (highlighted in red, *left*). Despite this, the tiling remains deployable, as shown by the yellow paper fabrication, though the opening angles are not congruent.

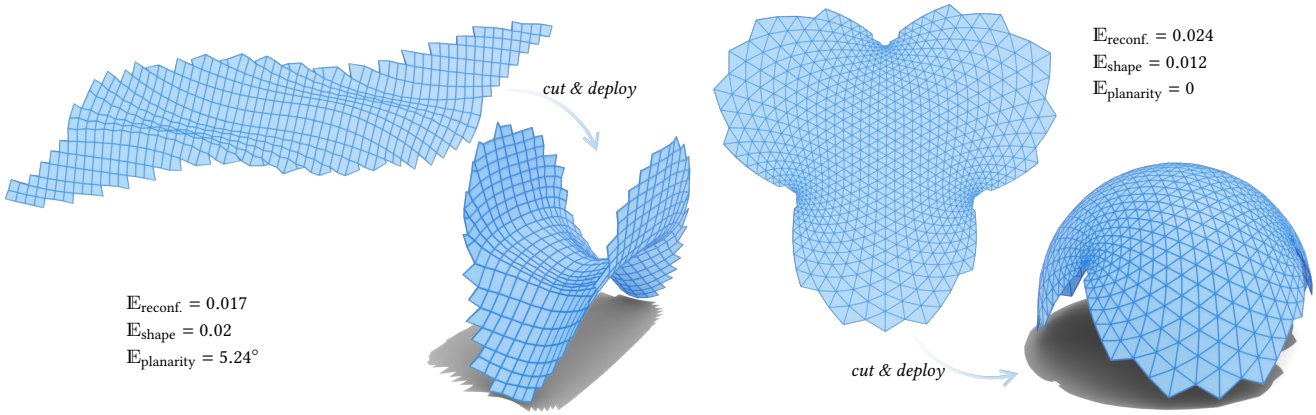

Fig. F.4. Failure cases: using the quad and triangle pattern to realize a pringle (left) and hemisphere (right) shape. We report the *maximal* values for the reconfigurability, shape approximation and planarity errors. Although the shape approximation appears reasonable, the non-negligible reconfigurability and planarity errors make fabrication difficult, if not impossible.

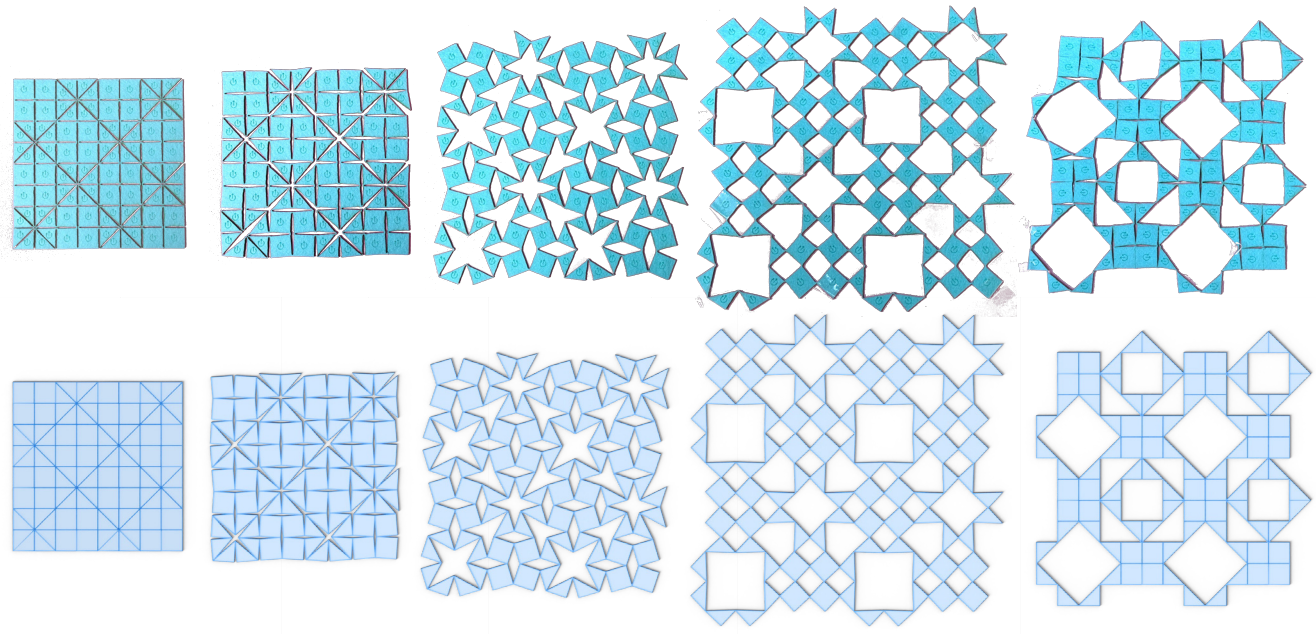

Fig. F.5. For the tiling in Fig. 5, we show the intermediate deployment states from real-world fabrication (*top* row, laser-cut felt) and simulated results at similar stages (*bottom*).

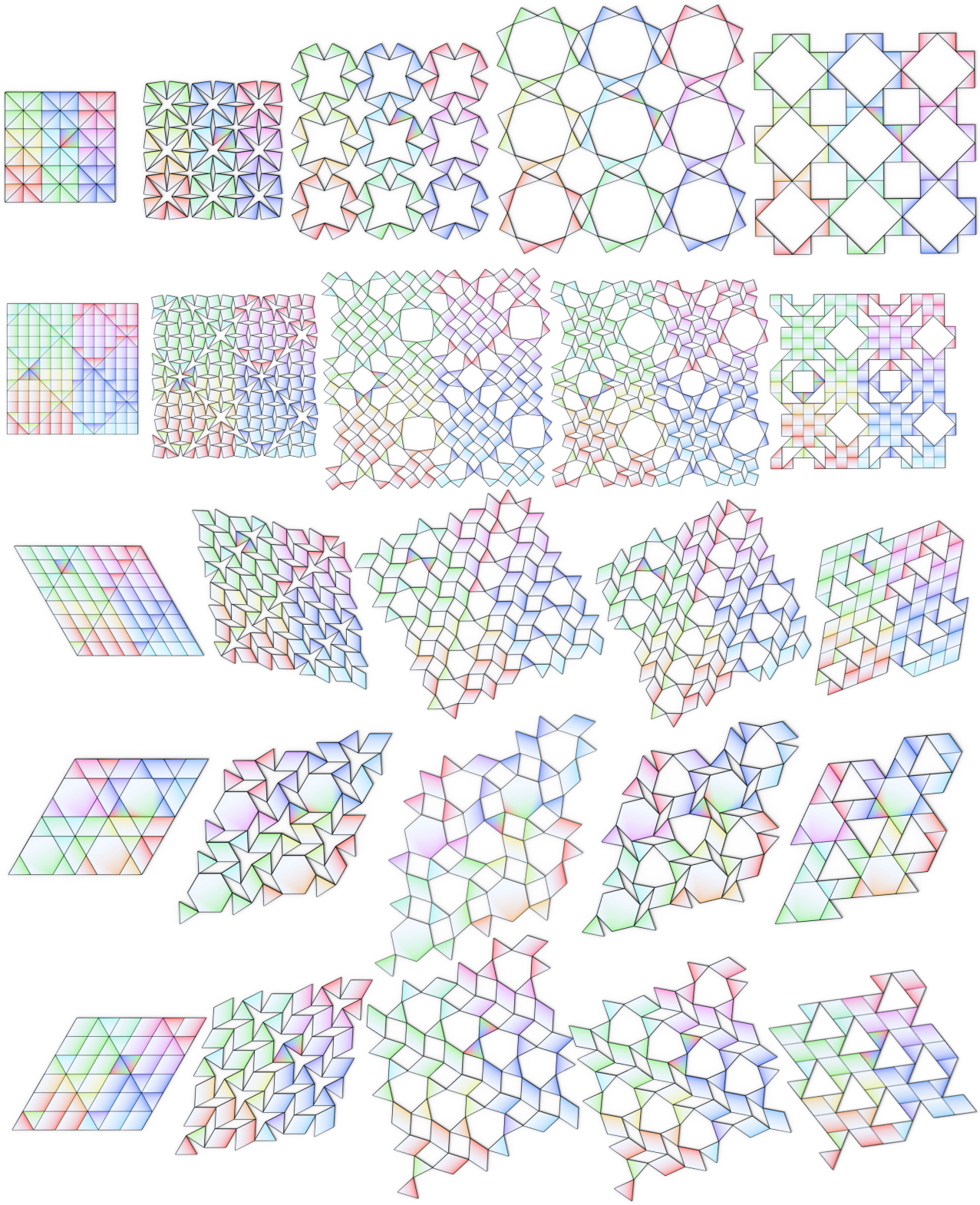

Fig. F.6. For the tilings in Fig. 13 of the main paper, we show the deployment process of the unoptimized regular patterns. We color the corresponding faces in different stages using the same color scheme, applied in a gradient style, to facilitate the observation of their rotations.

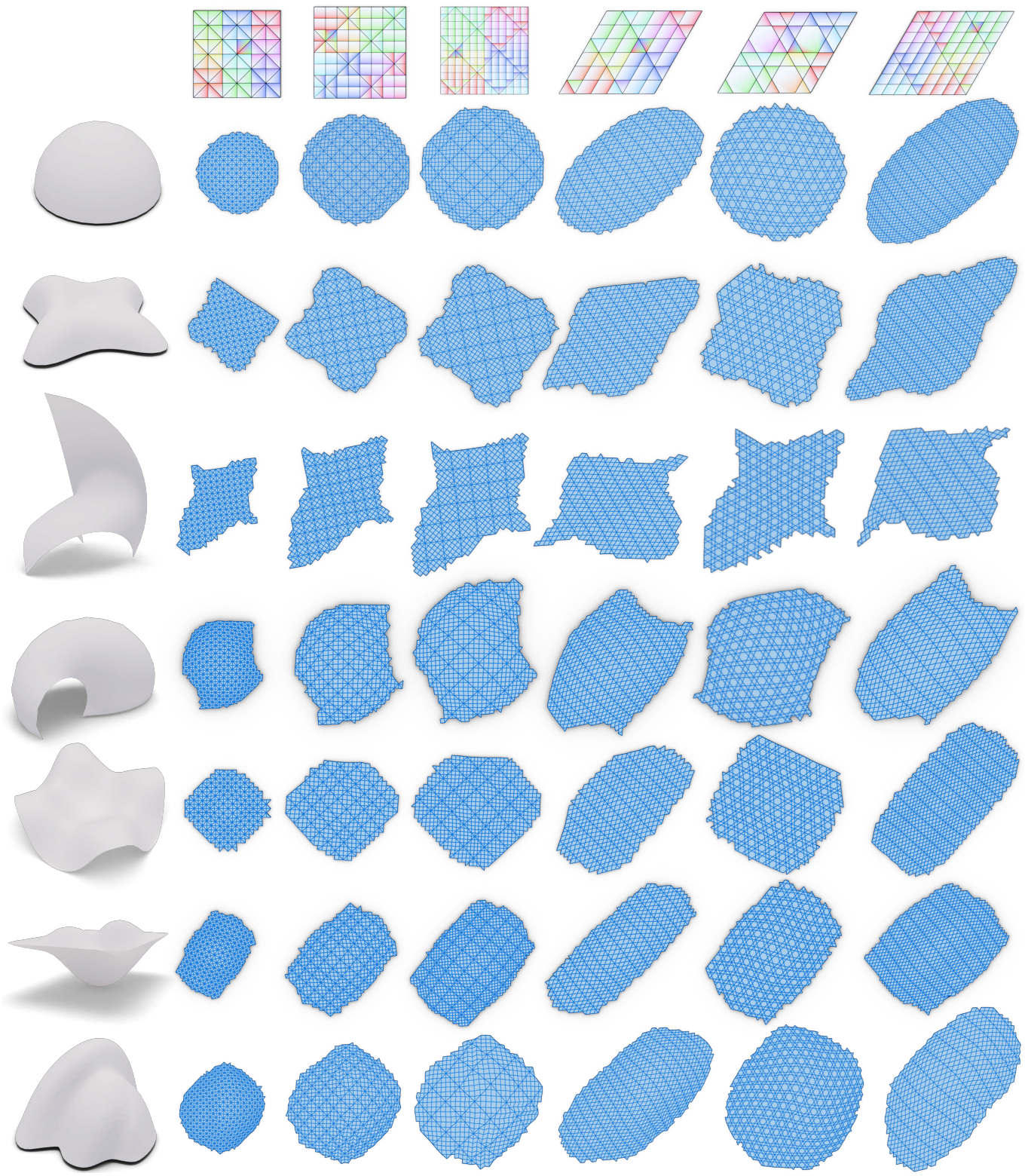

Fig. F.7. For the deployed results shown in Fig. 13, we display their corresponding optimized tilings prior to deployment. For each shape (i.e., each row), the scales of the tiles are consistent and comparable. For example, the first tiling exhibits much larger holes after deployment compared to other patterns, so its optimized tiling requires a relatively smaller area.

Table F.1. For the target shapes shown in Fig. 13, namely *Hemisphere* ($\mathcal{M}_1$), *Lilium* ($\mathcal{M}_2$), *Pringle shell* ($\mathcal{M}_3$), *Shell* ($\mathcal{M}_4$), *Wavy plane* ($\mathcal{M}_5$), *Bumpy plane* ($\mathcal{M}_6$) and *Botanic garden* ($\mathcal{M}_7$), and for each pattern shown in columns, we report the number of vertices in the pattern before and after deployment ($n_{v,2d}$ and $n_{v,3d}$, respectively), the number of faces (n_f), the average reconfigurability error ($\mathbb{E}_r$), shape approximation error ($\mathbb{E}_s$) and planarity error in degrees for polygonal faces only ($\mathbb{E}_p$). Additionally, we provide the runtime (t) until convergence, measured in milliseconds.

patterns		***pattern 1***							***pattern 2***							***pattern 3***						
target geometry		M_1	M_2	M_3	M_4	M_5	M_6	M_7	M_1	M_2	M_3	M_4	M_5	M_6	M_7	M_1	M_2	M_3	M_4	M_5	M_6	M_7
#var	$n_{v,2d}$	400	279	302	459	284	380	897	693	524	612	575	462	654	1791	865	759	648	739	761	1141	3010
	$n_{v,3d}$	937	646	689	1078	647	879	2158	1244	941	1087	1027	828	1169	3285	1359	1184	1001	1148	1172	1794	4772
	n_f	724	487	525	830	495	678	1689	960	716	826	781	632	894	2565	1075	933	776	901	926	1424	3860
err.	$\mathbb{E}_r$ ($\times 10^{-4}$)	8.25	0.43	0.70	2.00	1.97	5.54	14.37	7.76	0.73	0.61	1.58	1.12	5.59	11.26	6.71	0.93	0.71	1.55	1.27	6.67	7.72
	$\mathbb{E}_s$ ($\times 10^{-4}$)	5.46	0.33	0.09	15.47	1.05	4.54	36.85	6.66	7.04	1.98	145.1	7.19	13.56	71.67	9.22	14.91	3.70	235.2	12.39	17.10	74.02
	$\mathbb{E}_p$ ($\circ$)	0	0	0	0	0	0	0	0.018	0.019	0.0115	0.013	0.011	0.013	0.006	0.022	0.027	0.015	0.020	0.020	0.011	0.018
t (ms)		80	100	50	127	95	79	319	303	539	582	318	334	1319	4077	1546	10995	2455	1654	2754	250	463

patterns		***pattern 4***							***pattern 5***							***pattern 6***						
target geometry		M_1	M_2	M_3	M_4	M_5	M_6	M_7	M_1	M_2	M_3	M_4	M_5	M_6	M_7	M_1	M_2	M_3	M_4	M_5	M_6	M_7
#var	$n_{v,2d}$	684	660	599	795	590	634	1009	867	719	804	887	957	1018	1600	1538	1187	616	692	1059	1100	1581
	$n_{v,3d}$	1101	1057	960	1274	940	1015	1628	1266	1045	1167	1292	1395	1485	2356	2262	1736	892	1007	1549	1619	2320
	n_f	841	805	720	975	715	768	1251	1006	826	916	1027	1113	1188	1900	1820	1382	695	792	1235	1284	1866
err.	$\mathbb{E}_r$ ($\times 10^{-4}$)	3.75	1.98	1.78	2.34	2.48	3.94	6.91	3.68	1.25	0.82	3.67	1.99	4.06	7.30	6.57	1.64	1.63	3.40	2.43	5.94	9.91
	$\mathbb{E}_s$ ($\times 10^{-4}$)	14.91	16.81	5.41	223.2	18.46	23.69	170.0	14.77	19.89	4.32	277.5	14.79	20.30	144.0	14.25	17.24	8.67	395.7	17.82	28.45	201.8
	$\mathbb{E}_r$($\circ$)	0.037	0.024	0.021	0.019	0.026	0.019	0.010	0.027	0.027	0.021	0.021	0.023	0.025	0.015	0.022	0.023	0.017	0.018	0.023	0.004	0.014
t (ms)		346	862	694	827	116	1533	2821	293	784	399	697	579	652	6243	5240	5515	15985	3525	7666	222	1170

Table F.2. Statistics for the shapes with negative curvatures (denoted as N_1, N_2, N_3, N_4) and positive curvatures (denoted as P_1, P_2, P_3, P_4) shown in Fig. 14.

patterns		**negative curvature (Fig. 14a)**								**positive curvature (Fig. 14a)**							
		pattern 1 (first row)				***pattern 2 (second row)***				***pattern 1 (first row)***				***pattern 2 (second row)***			
target geometry		N_1	N_2	N_3	N_4	N_1	N_2	N_3	N_4	P_1	P_2	P_3	P_4	P_1	P_2	P_3	P_4
#var	$n_{v,2d}$	357	428	401	465	443	462	508	445	798	776	764	836	817	803	803	894
	$n_{v,3d}$	550	664	629	722	637	663	728	639	1248	1212	1190	1308	1183	1164	1169	1301
	n_f	425	515	487	561	498	519	571	498	990	959	941	1034	941	925	932	1041
err.	$\mathbb{E}_r$($\times 10^{-4}$)	0.62	1.10	1.97	1.01	0.84	1.36	1.21	2.77	1.14	6.18	11.53	1.99	0.51	2.40	8.09	1.70
	$\mathbb{E}_s$($\times 10^{-4}$)	31.17	33.78	45.22	42.65	18.31	17.81	21.35	26.17	4.79	7.88	11.93	11.07	5.46	7.93	13.09	15.21
	$\mathbb{E}_p$($\circ$)	0.037	0.020	0.017	0.033	0.018	0.032	0.020	0.005	0.019	0.016	0.012	0.013	0.019	0.019	0.0134	0.019
t (ms)		1775	6011	5180	4799	87	115	180	374	832	1153	1879	85	149	181	439	240